

High-Order Multirate Explicit Time-Stepping Schemes for the Baroclinic-Barotropic Split Dynamics in Primitive Equations

Rihui Lan^a, Lili Ju^{a,*}, Zhu Wang^a, Max Gunzburger^b, Philip Jones^c

^a*Department of Mathematics, University of South Carolina, Columbia, SC 29208, USA*

^b*Department of Scientific Computing, Florida State University, Tallahassee, FL 32306, USA*

^c*Theoretical Division, Los Alamos National Laboratory, Los Alamos, NM 87545, USA*

Abstract

In order to treat the multiple time scales of ocean dynamics in an efficient manner, the baroclinic-barotropic splitting technique has been widely used for solving the primitive equations for ocean modeling. In this paper, we propose second and third-order multirate explicit time-stepping schemes for such split systems based on the strong stability-preserving Runge-Kutta (SSPRK) framework. Our method allows for a large time step to be used for advancing the three-dimensional (slow) baroclinic mode and a small time step for the two-dimensional (fast) barotropic mode, so that each of the two mode solves only need satisfy their respective CFL condition to maintain numerical stability. It is well known that the SSPRK method achieves high-order temporal accuracy by utilizing a convex combination of forward-Euler steps. At each time step of our method, the baroclinic velocity is first computed by using the SSPRK scheme to advance the baroclinic-barotropic system with the large time step, then the barotropic velocity is specially corrected by using the same SSPRK scheme with the small time step to advance the barotropic subsystem with a barotropic forcing interpolated based on values from the preceding baroclinic solves. Finally, the fluid thickness and the sea surface height perturbation is updated by coupling the predicted baroclinic and barotropic velocities. Temporal truncation error analyses are also carried out for the proposed schemes. Two benchmark tests drawn from the “MPAS-Ocean” platform are used to numerically demonstrate the accuracy and parallel performance of the proposed schemes.

Keywords: Primitive equations, baroclinic-barotropic splitting, explicit time-stepping, multirate, strong stability-preserving Runge-Kutta

1. Introduction

The importance of the ocean to our everyday lives, now and more so in the future, is undeniable because it has a huge impact on the climate. To better understand and forecast the ocean and its effect on climate, a number of computational models, based on fundamental physics laws and the properties of geophysical flows, have been developed and used in practical applications. Among them are the primitive equations [1, 2, 3] which are a simplification of the Navier-Stokes equations. Those equations couple tracers such as temperature, salinity, and chemicals to the fluid velocity, depth (or layer thickness), and pressure. The shallow-water equations [4, 3, 5] which are a further

*Corresponding author

Email addresses: rlan@mailbox.sc.edu (Rihui Lan), ju@math.sc.edu (Lili Ju), wangzhu@math.sc.edu (Zhu Wang), mgunzburger@fsu.edu (Max Gunzburger), pwjones@lanl.gov (Philip Jones)

simplification, are often employed in some specific circumstances such as for flows in rivers and coastal areas. Due to the high horizontal-to-vertical aspect ratio of the ocean, models are generally derived by modeling the fluid as a single layer or as a stack of immiscible layers, each having a uniform fluid density. Consequently, layered models are ideal for modeling stratified fluid flows and perform well at portraying vertical profiles. For additional details, the reader may refer to [6, 3] and the references cited therein.

Numerical simulations of the layered models are still challenging due to the massive computational complexity caused by integrating the large-scale dynamical system. Because external and internal gravity waves and the Earth’s rotation are intertwined, ocean dynamics often involves several time scales. Explicit time-stepping schemes have been popularly applied in many numerical ocean models due to their natural parallelism and ease of implementation. However, in order to achieve stable numerical simulations, such schemes have to use quite small time-step sizes imposed by the Courant-Friedrichs-Lewy (CFL) condition for the fastest time scales of the dynamics. This renders numerical simulations to be computationally expensive, especially for long-term predictions. Therefore, it is natural to separate the scales having different characteristic time scales and advance them using different time-step sizes. There are available two common approaches to accomplish this goal. One approach are explicit local time-stepping (LTS) schemes [7, 8, 9, 10]. Because CFL conditions vary greatly over the whole ocean domain, LTS methods apply spatially-dependent time-step sizes on different subdomains to achieve better efficiency compared to that obtained using globally uniform time-stepping methods. The other approach are multirate time-stepping schemes [11, 12, 13, 14] that are based on splitting the ocean dynamics. A large time-step size is used when advancing the slow dynamics modes and a small step size (i.e., substepping) is used when solving for the fast dynamics mode, so that each of the mode solves only needs to satisfy their respective CFL condition for numerical stability. In this paper, we focus on a novel instance of the latter approach, namely we study high-order multirate time-stepping schemes for the primitive equations.

Among the fast components of the primitive equations, the barotropic mode is the fastest of the entire spectrum of inertial-gravity waves. It has been a standard practice in ocean modeling to split that mode from the rest of the waves that make up the baroclinic mode. Based on the baroclinic-barotropic splitting, split-explicit (SE) time integration schemes have been developed in [11, 15, 16, 13, 14, 17, 18, 19]. In those approaches, the barotropic velocity is obtained via the mass-weighted vertical averaging and the baroclinic velocity consists of the difference between the original velocity and the barotropic one. The whole dynamic system is then divided into a two-dimensional barotropic subsystem for the fast barotropic gravity wave and a three-dimensional baroclinic subsystem for the slow baroclinic mode. This splitting idea is used in [11] to numerically predict the Atlantic ocean under the isopycnic coordinate system. However, in [20] it was discovered that the scheme developed in [11] was not stable due to a certain inexactness in the splitting. Subsequently, a more stable two-level time-stepping method was proposed in [17]. Furthermore, the splitting method was generalized to multi-layer ocean models in [12, 13, 14]. In particular, the barotropic mode in these methods is obtained by averaging the momentum equation. For simplicity, only the linear Coriolis term and the gradient of the mass-weighted Montgomery potential are kept; all the other terms are then gathered in a special forcing term $\overline{\mathbf{G}}$ (usually called “barotropic forcing”). Without accessing its (complicated) explicit formula, the value of $\overline{\mathbf{G}}$ is calculated efficiently from the baroclinic subsystem by using the mass-weighted free condition, so that $\overline{\mathbf{G}}$ can bridge the baroclinic and barotropic modes. Furthermore, in [14], a forward-backward substepping solver for the fast barotropic subsystem with $\overline{\mathbf{G}}$ calculated by the baroclinic mode. This two-level SE time-stepping approach has been implemented in some ocean model software packages, such as “MPAS-Ocean” [21], a numerical ocean model developed at the Los Alamos National Laboratory and its collaborating institutions for the simulation of the ocean system across scales on staggered

C-grids. This model was developed for use in the Energy Exascale Earth System Model (E3SM; [22]) as well as in some ocean-only applications [23, 24, 25, 26]. Implementation details about the MPAS-SE are given in [27]. The MPAS-SE package is based on the numerical schemes developed in [21, 28, 29] where it is shown how the MPAS-SE scheme improves the efficiency of ocean simulations. However, the MPAS-SE scheme seems to have only first-order accuracy in time as is verified by our experiments in this paper.

For the efficiently handling of the multiple time scales while simultaneously achieving higher-order accuracy for a given system, some variants of the Runge-Kutta methods have been developed. In [30], the multirate partitioned Runge-Kutta (MPRK) method was proposed and order conditions were derived based on the P-series [31]. Recently, in [32, 33], a generalized additive Runge-Kutta (GARK) method was designed which allows the evolution of the fast and slow modes using different numbers of stages and distinct sizes of time steps. However, neither the MPRK nor the GARK are directly applicable to the baroclinic-barotropic split system of the primitive equations for ocean modeling. The main issue is that one would have to compute the barotropic forcing $\overline{\mathbf{G}}$ for each substep that advances the barotropic subsystem at all stages of MPRK or GARK, but the explicit form of $\overline{\mathbf{G}}$ is difficult to access in this case. Some other classic high-order time-stepping schemes have also been adopted in existing numerical ocean models [34], including Leap-Frog, Adams-Bashforth, and forward-backward algorithms. In addition, the TVD (total variation diminishing) [35, 36, 37] and SSPRK (strong stability preserving Runge-Kutta) [38, 39] methods have attracted some attention. In [40], TVD limiters were considered for the advection of temperature and salinity in ocean modeling. In [41], SSPRK method was applied for the Boussinesq model to model wave shoaling, breaking, wave run-up, and wave-averaged nearshore circulation. In [42], the SSPRK method was used with horizontally explicit, vertically implicit schemes to solve the compressible Boussinesq equations.

In this paper we propose high-order multirate explicit time-stepping schemes, based on the SSPRK framework, for solving the baroclinic-barotropic split system of primitive equations. The SSPRK schemes are well known to achieve high-order temporal accuracy by utilizing a convex combination of forward-Euler steps. Using this framework, we are able to compute the barotropic forcing term $\overline{\mathbf{G}}$ efficiently using the approach of [13] at each stage of the SSPRK schemes. In particular, at each time step, the baroclinic velocity is first computed by using the SSPRK scheme to advance the baroclinic-barotropic system with the large time step, then the barotropic velocity is specially corrected by using the same SSPRK scheme with the smaller time step to advance the barotropic subsystem with a barotropic forcing term interpolated based on values from the preceding forward-Euler baroclinic solves, and finally the fluid thickness and the sea surface height perturbation are updated by coupling the predicted baroclinic and barotropic velocities.

The rest of paper is structured as follows. In Section 2, we review the primitive equations and the corresponding baroclinic-barotropic dynamics splitting. Next, in Section 3, we present second and third-order multirate time-stepping schemes for the baroclinic-barotropic split system. Truncation error analyses in time are then carried out in Section 4. In Section 5, numerical experiments based on benchmark test cases from the “MPAS-Ocean” platform are investigated to demonstrate the accuracy and parallel performance of the proposed schemes. Finally, some concluding remarks are given in Section 6.

2. The primitive equations and the baroclinic-barotropic dynamics splitting

We consider oceanic flows as governed by the following primitive equations for L layers in the z -level vertical coordinate: for $k = 1, 2, \dots, L$,

- thickness equation:

$$\frac{\partial h_k}{\partial t} + \nabla \cdot (h_k \mathbf{u}_k) + \frac{\partial}{\partial z} (h_k w_k) = 0, \quad (1)$$

- momentum equation:

$$\frac{\partial \mathbf{u}_k}{\partial t} + \frac{1}{2} \nabla |\mathbf{u}_k|^2 + (\mathbf{k} \cdot \nabla \times \mathbf{u}_k) \mathbf{u}_k^\perp + f \mathbf{u}_k^\perp + w_k \frac{\partial \mathbf{u}_k}{\partial z} = -\frac{1}{\rho_0} \nabla p_k + \nu_h \nabla^2 \mathbf{u}_k + \frac{\partial}{\partial z} (\nu_v \frac{\partial \mathbf{u}_k}{\partial z}), \quad (2)$$

- tracer equations:

$$\frac{\partial h_k \varphi_k}{\partial t} + \nabla \cdot (h_k \varphi_k \mathbf{u}_k) + \frac{\partial}{\partial z} (h_k \varphi_k w_k) = \nabla \cdot (h_k \kappa_h \nabla \varphi_k) + h_k \frac{\partial}{\partial z} (\kappa_v \frac{\partial \varphi_k}{\partial z}), \quad (3)$$

- hydrostatic condition:

$$p_k = p_k^s(x, y) + \int_z^{z_k^s} \rho g dz'. \quad (4)$$

- equation of state:

$$\rho_k = f_{\text{eos}}(\Theta, S, p), \quad (5)$$

where the definitions of the variables involved are listed in Table 1.

Variables	Definition
h_k	k th-layer thickness
h	Layer thickness containing all the layers
\mathbf{u}_k, w_k	Horizontal and vertical velocity in layer k
\mathbf{u}, w	Horizontal and vertical velocity containing all the layers
$p_k, p_k^s(x, y)$	Pressure and the pressure at the top of layer k
Θ	Potential temperature
S	Salinity
ρ_k, ρ_0	Density and reference density
φ_k	Generic tracer (Θ or S)
z, z_k^s	Vertical coordinate and the z -location of the top boundary of layer k
ν_h, ν_v	Viscosities
κ_h, κ_v	Tracer diffusion coefficients
f, g	Coriolis parameter and gravitational constant
\mathbf{k}	Unit vector point in the local vertical direction
L	Number of layers

Table 1: List of variables and other entities for the primitive equations (1)-(5).

Remark 2.1. In (2), a Laplacian form of horizontal diffusion is shown. Often, this is replaced by alternative formulations or turbulent closures for horizontal dissipation. Specifically, the hyper-viscosity $-\nu_h \nabla^4 \mathbf{u}_k$ will be considered instead of $\nu_h \nabla^2 \mathbf{u}_k$ because it provides a more scale-selective dissipation effect.

In the following, we will concentrate on designing high-order time integration schemes for the ocean dynamics part of the primitive equations, i.e., the thickness and momentum equations (1)-(2) coupled with the hydrostatic condition (4), which together are the key component in numerical ocean modeling. Because the dynamics involves scales having different characteristic times, it is a widespread practice to recognize the fast and slow motions, and split the momentum equation into

barotropic and baroclinic subsystems. Define the barotropic and baroclinic velocities by $\bar{\mathbf{u}}$ and $\tilde{\mathbf{u}}_k$, respectively, by [11]:

$$\begin{cases} \bar{\mathbf{u}} = \sum_{k=1}^L h_k \mathbf{u}_k / \sum_{k=1}^L h_k, \\ \tilde{\mathbf{u}}_k = \mathbf{u}_k - \bar{\mathbf{u}}, \quad k = 1, \dots, L. \end{cases} \quad (6)$$

For simplicity of exposition, we also set the quantities \mathbf{T}_k^u , \mathbf{D}_k^u and \mathbf{T}_k^h to be

$$\begin{aligned} \mathbf{T}_k^u(\mathbf{u}) &= -\frac{1}{2} \nabla |\mathbf{u}_k|^2 - (\mathbf{k} \cdot \nabla \times \mathbf{u}_k) \mathbf{u}_k^\perp - w_k \frac{\partial \mathbf{u}_k}{\partial z} - \frac{1}{\rho_0} \nabla p_k + \nu_h \nabla^2 \mathbf{u}_k, \\ \mathbf{D}_k^u(\mathbf{u}) &= \frac{\partial}{\partial z} (\nu_v \frac{\partial \mathbf{u}_k}{\partial z}), \\ \mathbf{T}_k^h(h, \mathbf{u}) &= -\nabla \cdot (h_k \mathbf{u}_k) - \frac{\partial}{\partial z} (h_k w_k). \end{aligned}$$

Taking the layer-thickness-weighted average of (2), one then can reformulate the dynamics of the primitive equations into the following baroclinic-barotropic split system:

$$\text{Baroclinic mode:} \quad \frac{\partial \tilde{\mathbf{u}}_k}{\partial t} = -f \tilde{\mathbf{u}}_k^\perp + \mathbf{T}_k^u(\mathbf{u}) + \mathbf{D}_k^u(\mathbf{u}) + g \nabla \zeta - \bar{\mathbf{G}}, \quad (7a)$$

$$\text{Barotropic mode:} \quad \frac{\partial}{\partial t} \begin{pmatrix} \bar{\mathbf{u}} \\ \zeta \end{pmatrix} = - \begin{pmatrix} f \mathbf{k} \times \bar{\mathbf{u}} + g \nabla \zeta \\ \nabla \cdot (\bar{\mathbf{u}}(\zeta + H)) \end{pmatrix} + \begin{pmatrix} \bar{\mathbf{G}} \\ 0 \end{pmatrix}, \quad (7b)$$

$$\text{Fluid thickness:} \quad \frac{\partial h_k}{\partial t} = \mathbf{T}_k^h(h, \mathbf{u}), \quad (7c)$$

where ζ is the sea surface height (SSH) perturbation, H is the total column height (with respect to the SSH), and the barotropic forcing term $\bar{\mathbf{G}}$ contains all other nonlinear terms in the equations for the baroclinic and barotropic modes. It is easy to see that the baroclinic subsystem (7a) and the fluid thickness equations (7c) are three-dimensional problems because they involve all L layers whereas the barotropic subsystem (7b) is only a two-dimensional problem. The explicit formula for $\bar{\mathbf{G}}$ is quite complicated to represent, thus an elegant forward-Euler method was proposed in [13] for its numerical evaluation by imposing the layer-thickness-weighted average free condition for the baroclinic mode, which does not need use of the explicit formula.

Remark 2.2. *It is worth noting that the SSH perturbation ζ can be determined from the layer thickness h by using the definition $\zeta = \sum_{k=1}^L h_k - H$, but it also can be solved from the barotropic subsystem (7b). At the temporal-spatial continuous level, these two ways are obviously equivalent, but this equivalence does not hold anymore in the spatially discrete setting so that it causes ζ to be overdetermined. MPAS-Ocean suggests to use $\zeta = \sum_{k=1}^L h_k - H$ for updating the SSH perturbation during each time-stepping; we follow this approach.*

3. High-order multirate explicit time-stepping schemes for the split system

In order to accurately simulate the ocean dynamics, we develop efficient high-order multirate explicit time-stepping methods for solving the baroclinic-barotropic split system (7). Our method is based on the strong stability preserving Rung-Kutta (SSPRK) method [38, 39] with special treatments of the coupling of the fast and slow modes. In the following, we first review some classic SSPRK schemes, and then present our second and third-order multirate split-explicit schemes.

Consider the system of ODEs

$$\partial_t \mathbf{V} = F(\mathbf{V}), \quad (8)$$

where $\mathbf{V}(t)$ is a vector of unknown variables with $\mathbf{V}^0 = \mathbf{V}(0)$. Given \mathbf{V}^n at the current time t_n and the time-step size Δt , to find \mathbf{V}^{n+1} at the time $t_{n+1} = t_n + \Delta t$, the second and third-order SSPRK schemes (referred to as SSPRK2 and SSPRK3, respectively) use the following convex combinations of forward-Euler steps:

- SSPRK2 (two stages)

$$\begin{cases} \widehat{\mathbf{V}}^{n+1} = \mathbf{V}^n + \Delta t F(\mathbf{V}^n), \\ \mathbf{V}^{n+1} = \frac{1}{2} \mathbf{V}^n + \frac{1}{2} (\widehat{\mathbf{V}}^{n+1} + \Delta t F(\widehat{\mathbf{V}}^{n+1})). \end{cases}$$

- SSPRK3 (three stages)

$$\begin{cases} \widehat{\mathbf{V}}^{n+1} = \mathbf{V}^n + \Delta t F(\mathbf{V}^n), \\ \widehat{\mathbf{V}}^{n+1/2} = \frac{3}{4} \mathbf{V}^n + \frac{1}{4} (\widehat{\mathbf{V}}^{n+1} + \Delta t F(\widehat{\mathbf{V}}^{n+1})), \\ \mathbf{V}^{n+1} = \frac{1}{3} \mathbf{V}^n + \frac{2}{3} (\widehat{\mathbf{V}}^{n+1/2} + \Delta t F(\widehat{\mathbf{V}}^{n+1/2})). \end{cases}$$

We fit the baroclinic-barotropic split system (7) into the above SSPRK framework with the goal being to develop high-order multirate explicit time-stepping schemes that could evolve the baroclinic mode by a large time-step size and the barotropic mode by a smaller step size.

3.1. Forward-Euler stepping for the baroclinic mode

The baroclinic and barotropic modes represent the two different time scales of the ocean dynamics system and thus correspond to different CFL conditions. The former usually admits a large time-step size for stepping, whereas the latter generally requires a small time-step size, but we must take careful care of the coupling between these two modes in order to design overall numerical schemes of high-order accuracy. In particular, the barotropic forcing term $\overline{\mathbf{G}}$ plays a vital role in their coupling in the split system (7). To avoid using the explicit formula of $\overline{\mathbf{G}}$, it was proposed in [14] that an efficient way to calculate this term when the forward-Euler stepping is used for solving the baroclinic subsystem (7a); this approach is summarized in Algorithm 1. In the sequel, we refer this process as

$$\left[\widehat{\mathbf{u}}^{n+1}, \overline{\mathbf{G}}^n \right] = \text{Baroclinic_FEuler}(\mathbf{u}^n, \tilde{\mathbf{u}}^n, \zeta^n, h^n, \Delta t). \quad (9)$$

Algorithm 1: Baroclinic_FEuler

Input: $\mathbf{u}^n, \tilde{\mathbf{u}}^n, \zeta^n, h^n, \Delta t$

Output: $\widehat{\mathbf{u}}^{n+1}, \overline{\mathbf{G}}^n$

$$\widehat{\mathbf{u}}_k^{n+1} = \tilde{\mathbf{u}}_k^n + \Delta t \left(-f \tilde{\mathbf{u}}_k^{n,\perp} + \mathbf{T}_k^u(\mathbf{u}^n) + \mathbf{D}_k^u(\mathbf{u}^n) + g \nabla \zeta^n \right), \quad k = 1, \dots, L$$

$$\overline{\mathbf{G}}^n = \frac{1}{\Delta t} \sum_{k=1}^L h_k^n \widehat{\mathbf{u}}_k^{n+1} / \sum_{k=1}^L h_k^n$$

$$\widehat{\mathbf{u}}_k^{n+1} = \tilde{\mathbf{u}}_k^{n+1} - \Delta t \overline{\mathbf{G}}^n, \quad k = 1, \dots, L$$

In some ocean modeling situations, the vertical motion is stiffer than the horizontal motion due to the much smaller vertical mesh sizes compared with the horizontal ones. A “vertical mixing”

technique could be applied to tackle this issue, treating the vertical diffusion term $D_k^u(\mathbf{u})$ implicitly in (7a) (essentially a first-order operator splitting technique). Considering the boundary conditions, such as the bottom drag, we perform the vertical mixing on the whole velocity \mathbf{u} instead of only on the baroclinic velocity $\tilde{\mathbf{u}}$; our approach is summarized in Algorithm 2 and is referred to as

$$\left[\widehat{\mathbf{u}}^{n+1}, \overline{\mathbf{G}}^n\right] = \text{Baroclinic_FEuler_Mixing}(\mathbf{u}^n, \tilde{\mathbf{u}}^n, \overline{\mathbf{u}}^n, \zeta^n, h^n, \Delta t). \quad (10)$$

Algorithm 2: Baroclinic_FEuler_Mixing

Input: $\mathbf{u}^n, \tilde{\mathbf{u}}^n, \overline{\mathbf{u}}^n, \zeta^n, h^n, \Delta t$

Output: $\widehat{\mathbf{u}}^{n+1}, \overline{\mathbf{G}}^n$

$$\widehat{\mathbf{u}}_k^{n+1} = \tilde{\mathbf{u}}_k^n + \Delta t \left(-f \tilde{\mathbf{u}}_k^{n,\perp} + \mathbf{T}_k^u(\mathbf{u}^n) + g \nabla \zeta^n \right), \quad k = 1, \dots, L$$

$$\overline{\mathbf{G}}^n = \frac{1}{\Delta t} \sum_{k=1}^L h_k^n \widehat{\mathbf{u}}_k^{n+1} / \sum_{k=1}^L h_k^n$$

$$\widehat{\mathbf{u}}_k^{n+1} = \widehat{\mathbf{u}}_k^{n+1} - \Delta t \overline{\mathbf{G}}^n, \quad k = 1, \dots, L$$

$$\widehat{\mathbf{u}}^{n+1} - \Delta t \mathbf{D}_k^u(\widehat{\mathbf{u}}^{n+1}) = \widehat{\mathbf{u}}_k^{n+1} + \overline{\mathbf{u}}^n \quad // \text{ Vertical diffusion solve}$$

$$\widehat{\mathbf{u}}_k^{n+1} = \widehat{\mathbf{u}}^{n+1} - \overline{\mathbf{u}}^n$$

When one uses the Forward-Euler scheme with vertical mixing for advancing the baroclinic subsystem (7a) (i.e., Algorithm 2 instead of Algorithm 1), the vertical diffusion equation involving $\widehat{\mathbf{u}}^{n+1}$ is solved implicitly. The resulting linear system consists of blocks of tridiagonal coefficient submatrices after the spatial discretization by the TRiSK scheme used in MAPS-Ocean, thus it can be efficiently solved via a tridiagonal matrix algorithm [43] along each independent vertical direction. Consequently, the vertical mixing does not appreciably decrease the performance of explicit time-stepping as shown in the Community Vertical Mixing Project (CVMix) [44]. On the other hand, we also note that the use of such a treatment could theoretically and practically degrade the high-order accuracies (down to 1 in the worst-case scenario) of the time-stepping schemes we propose in the paper when the effect of the vertical diffusion term $D_k^u(\mathbf{u})$ on the whole system is very strong. Algorithm 1 (or Algorithm 2 if wanted) will be repeatedly used in constructing our SSPRK-based higher-order multirate explicit time-stepping schemes and producing the needed values of the barotropic forcing term $\overline{\mathbf{G}}$.

3.2. SSPRK2-based multirate split-explicit scheme

The proposed SSPRK2-based multirate explicit time-stepping scheme for solving the baroclinic-barotropic split system (7) (referred to as ‘‘SSPRK2-SE’’) consists of three steps at each time-stepping from t_n to t_{n+1} . A SSPRK2 substepping process for the barotropic subsystem (7b) needs to be performed at Step 2 to compute the correct barotropic velocity, which is described in Algorithm 3, where M denotes the number of total substeps (i.e., the small time-step size is set to $\Delta t/M$), $\overline{\mathbf{G}}^n$ and $\overline{\mathbf{G}}^{n+1}$ are computed values from the two forward-Euler baroclinic solves at Step 1 and

$$\text{Eval}_2(\overline{\mathbf{G}}^n, \overline{\mathbf{G}}^{n+1}) = \frac{1}{2} \overline{\mathbf{G}}^n + \frac{1}{2} \overline{\mathbf{G}}^{n+1}. \quad (11)$$

We refer to it as

$$\left[\overline{\mathbf{u}}^{n+1}\right] = \text{Barotropic_SSPRK2_Substepping}\left(\overline{\mathbf{u}}^n, \zeta^n, \overline{\mathbf{G}}^n, \overline{\mathbf{G}}^{n+1}, \Delta t, M\right). \quad (12)$$

At a preprocessing phase, $\overline{\mathbf{u}}^0$ and $\tilde{\mathbf{u}}^0$ are computed from \mathbf{u}^0 using the splitting formula (6). Then at each time-stepping from t_n to t_{n+1} , the proposed SSPRK2-SE scheme reads as follows:

Algorithm 3: Barotropic_SSPRK2_Substepping

Input: $\bar{\mathbf{u}}^n, \zeta^n, \bar{\mathbf{G}}^n, \bar{\mathbf{G}}^{n+1}, \Delta t, M$

Output: $\bar{\mathbf{u}}^{n+1}$

$\bar{\mathbf{u}}^{n+0/M} \leftarrow \bar{\mathbf{u}}^n, \zeta^{n+0/M} \leftarrow \zeta^n$

for $j = 1$ **to** M **do**

$$\begin{cases}
 \widehat{\mathbf{u}}^{n+j/M} = \bar{\mathbf{u}}^{n+(j-1)/M} - \frac{\Delta t}{M} \left(f\mathbf{k} \times \bar{\mathbf{u}}^{n+(j-1)/M} + g\nabla\zeta^{n+(j-1)/M} - \text{Eval}_2(\bar{\mathbf{G}}^n, \bar{\mathbf{G}}^{n+1}) \right) \\
 \widehat{\zeta}^{n+j/M} = \zeta^{n+(j-1)/M} - \frac{\Delta t}{M} \nabla \cdot \left(\bar{\mathbf{u}}^{n+(j-1)/M} (\zeta^{n+(j-1)/M} + H) \right) \\
 \widehat{\mathbf{u}}^{n+(j+1)/M} = \widehat{\mathbf{u}}^{n+j/M} - \frac{\Delta t}{M} \left(f\mathbf{k} \times \widehat{\mathbf{u}}^{n+j/M} + g\nabla\widehat{\zeta}^{n+j/M} - \text{Eval}_2(\bar{\mathbf{G}}^n, \bar{\mathbf{G}}^{n+1}) \right) \\
 \widehat{\zeta}^{n+(j+1)/M} = \widehat{\zeta}^{n+j/M} - \frac{\Delta t}{M} \nabla \cdot \left(\widehat{\mathbf{u}}^{n+j/M} (\widehat{\zeta}^{n+j/M} + H) \right) \\
 \bar{\mathbf{u}}^{n+j/M} = \frac{1}{2} \left(\bar{\mathbf{u}}^{n+(j-1)/M} + \widehat{\mathbf{u}}^{n+(j+1)/M} \right) \\
 \zeta^{n+j/M} = \frac{1}{2} \left(\zeta^{n+(j-1)/M} + \widehat{\zeta}^{n+(j+1)/M} \right)
 \end{cases}$$

- **Step 1.** Advance the baroclinic-barotropic system (7) from t_n using SSPRK2 with the large time-step size Δt to compute the baroclinic velocity $\tilde{\mathbf{u}}^{n+1}$ (note that the barotropic mode and the fluid thickness are also partly advanced with Δt for the purpose of assisting the calculations):

$$[\widehat{\mathbf{u}}^{n+1}, \bar{\mathbf{G}}^n] = \text{Baroclinic_FEuler}(\mathbf{u}^n, \tilde{\mathbf{u}}^n, \zeta^n, h^n, \Delta t). \quad (13a)$$

$$\widehat{\mathbf{u}}^{n+1} = \bar{\mathbf{u}}^n - \Delta t (f\mathbf{k} \times \bar{\mathbf{u}}^n + g\nabla\zeta^n - \bar{\mathbf{G}}^n). \quad (13b)$$

$$\begin{cases}
 \widehat{h}_k^{n+1} = h_k^n + \Delta t \mathbf{T}_k^h(h^n, \mathbf{u}^n), \\
 \widehat{\zeta}^{n+1} = \sum_{k=1}^L \widehat{h}_k^{n+1} - H, \\
 \widehat{\mathbf{u}}_k^{n+1} = \widehat{\mathbf{u}}^{n+1} + \widehat{\mathbf{u}}_k^{n+1}.
 \end{cases} \quad (13c)$$

$$\begin{cases}
 [\widehat{\mathbf{u}}^{n+2}, \bar{\mathbf{G}}^{n+1}] = \text{Baroclinic_FEuler}(\widehat{\mathbf{u}}^{n+1}, \widehat{\mathbf{u}}^{n+1}, \widehat{\zeta}^{n+1}, \widehat{h}^{n+1}, \Delta t), \\
 \tilde{\mathbf{u}}^{n+1} = \frac{1}{2} (\tilde{\mathbf{u}}^n + \widehat{\mathbf{u}}^{n+2}).
 \end{cases} \quad (14a)$$

- **Step 2.** Advance the barotropic subsystem (7b) with the interpolated barotropic forcing $\text{Eval}_2(\bar{\mathbf{G}})$ (11) from t_n using SSPRK2 with the small time-step size $\Delta t/M$ to compute the correct barotropic velocity $\bar{\mathbf{u}}^{n+1}$:

$$[\bar{\mathbf{u}}^{n+1}] = \text{Barotropic_SSPRK2_Substepping}(\bar{\mathbf{u}}^n, \zeta^n, \bar{\mathbf{G}}^n, \bar{\mathbf{G}}^{n+1}, \Delta t, M). \quad (14b)$$

- **Step 3.** Combining the predicted barotropic and baroclinic velocities ($\tilde{\mathbf{u}}^{n+1}$ and $\bar{\mathbf{u}}^{n+1}$) to continue advancing the fluid thickness (left part from Step 1) to obtain h_k^{n+1} and then update

the SSH perturbation ζ^{n+1} :

$$\begin{cases} \mathbf{u}_k^{n+1} = \bar{\mathbf{u}}^{n+1} + \tilde{\mathbf{u}}_k^{n+1}, \\ \hat{h}_k^{n+2} = \hat{h}_k^{n+1} + \Delta t \mathbf{T}_k^h(\hat{h}^{n+1}, \mathbf{u}^{n+1}), & h_k^{n+1} = \frac{1}{2}(h_k^n + \hat{h}_k^{n+2}), \\ \zeta^{n+1} = \sum_{k=1}^L h_k^{n+1} - H. \end{cases} \quad (14c)$$

The total cost of SSPRK2-SE per time step mainly consists of 2 times of forward-Euler baroclinic solve (i.e., $O(2LN)$) and M times of two forward-Euler barotropic solves (i.e., $O(2MN)$), where N denotes the number of unknowns per layer.

3.3. SSPRK3-based split-explicit scheme

The proposed SSPRK3-based multirate explicit time-stepping scheme for solving the baroclinic-barotropic split system (7) (referred to as ‘‘SSPRK3-SE’’) again consists of three steps at each time-stepping from t_n to t_{n+1} . Similarly, a SSPRK3 substepping process for the barotropic subsystem (7b) needs to be performed at Step 2 to compute the correct barotropic velocity, which is described in Algorithm 4, where $\bar{\mathbf{G}}^n$, $\bar{\mathbf{G}}^{n+1}$ and $\bar{\mathbf{G}}^{n+1/2}$ are computed values from the three forward-Euler baroclinic solves at Step 1 and

$$\text{Eval}_3(\bar{\mathbf{G}}^n, \bar{\mathbf{G}}^{n+1}, \bar{\mathbf{G}}^{n+1/2}) = \frac{1}{6}\bar{\mathbf{G}}^n + \frac{1}{6}\bar{\mathbf{G}}^{n+1} + \frac{2}{3}\bar{\mathbf{G}}^{n+1/2}. \quad (15)$$

We refer to it as

$$[\bar{\mathbf{u}}^{n+1}] = \text{Barotropic_SSPRK3_Substepping}(\bar{\mathbf{u}}^n, \zeta^n, \bar{\mathbf{G}}^n, \bar{\mathbf{G}}^{n+1}, \bar{\mathbf{G}}^{n+1/2}, \Delta t, M). \quad (16)$$

Algorithm 4: Barotropic_SSPRK3_Substepping

Input: $\bar{\mathbf{u}}^n, \zeta^n, \bar{\mathbf{G}}^n, \bar{\mathbf{G}}^{n+1}, \bar{\mathbf{G}}^{n+1/2}, \Delta t, M$

Output: $\bar{\mathbf{u}}^{n+1}$

$\bar{\mathbf{u}}^{n+0/M} \leftarrow \bar{\mathbf{u}}^n, \zeta^{n+0/M} \leftarrow \zeta^n$

for $j = 1$ **to** M **do**

$$\begin{cases} \hat{\bar{\mathbf{u}}}^{n+j/M} = \bar{\mathbf{u}}^{n+(j-1)/M} - \frac{\Delta t}{M} \left(f\mathbf{k} \times \bar{\mathbf{u}}^{n+(j-1)/M} + g\nabla\zeta^{n+(j-1)/M} - \text{Eval}_3(\bar{\mathbf{G}}^n, \bar{\mathbf{G}}^{n+1}, \bar{\mathbf{G}}^{n+1/2}) \right) \\ \hat{\zeta}^{n+j/M} = \zeta^{n+(j-1)/M} - \frac{\Delta t}{M} \nabla \cdot \left(\bar{\mathbf{u}}^{n+(j-1)/M} (\zeta^{n+(j-1)/M} + H) \right) \\ \hat{\bar{\mathbf{u}}}^{n+(j+1)/M} = \hat{\bar{\mathbf{u}}}^{n+j/M} - \frac{\Delta t}{M} \left(f\mathbf{k} \times \hat{\bar{\mathbf{u}}}^{n+j/M} + g\nabla\hat{\zeta}^{n+j/M} - \text{Eval}_3(\bar{\mathbf{G}}^n, \bar{\mathbf{G}}^{n+1}, \bar{\mathbf{G}}^{n+1/2}) \right) \\ \hat{\zeta}^{n+(j+1)/M} = \hat{\zeta}^{n+j/M} - \frac{\Delta t}{M} \nabla \cdot \left(\hat{\bar{\mathbf{u}}}^{n+j/M} (\hat{\zeta}^{n+j/M} + H) \right) \\ \hat{\bar{\mathbf{u}}}^{n+(j-1/2)/M} = \frac{3}{4}\bar{\mathbf{u}}^{n+(j-1)/M} + \frac{1}{4}\hat{\bar{\mathbf{u}}}^{n+(j+1)/M}, \hat{\zeta}^{n+(j-1/2)/M} = \frac{3}{4}\zeta^{n+(j-1)/M} + \frac{1}{4}\hat{\zeta}^{n+(j+1)/M} \\ \hat{\bar{\mathbf{u}}}^{n+(j+1/2)/M} = \\ \bar{\mathbf{u}}^{n+(j-1/2)/M} - \frac{\Delta t}{M} \left(f\mathbf{k} \times \bar{\mathbf{u}}^{n+(j-1/2)/M} + g\nabla\zeta^{n+(j-1/2)/M} - \text{Eval}_3(\bar{\mathbf{G}}^n, \bar{\mathbf{G}}^{n+1}, \bar{\mathbf{G}}^{n+1/2}) \right) \\ \hat{\zeta}^{n+(j+1/2)/M} = \zeta^{n+(j-1/2)/M} - \frac{\Delta t}{M} \nabla \cdot \left(\bar{\mathbf{u}}^{n+(j-1/2)/M} (\zeta^{n+(j-1/2)/M} + H) \right) \\ \bar{\mathbf{u}}^{n+j/M} = \frac{1}{3}\bar{\mathbf{u}}^{n+(j-1)/M} + \frac{2}{3}\hat{\bar{\mathbf{u}}}^{n+(j+1/2)/M}, \zeta^{n+j/M} = \frac{1}{3}\zeta^{n+(j-1)/M} + \frac{2}{3}\hat{\zeta}^{n+(j+1/2)/M} \end{cases}$$

At a preprocessing phase, $\bar{\mathbf{u}}^0$ and $\tilde{\mathbf{u}}^0$ are computed from \mathbf{u}^0 using the splitting formula (6). Then at each time step from t_n to t_{n+1} , the proposed SSPRK3-SE scheme read as follows:

- **Step 1.** Advance the baroclinic-barotropic system (7) from t_n using SSPRK3 with the large time-step size Δt to compute the baroclinic velocity $\tilde{\mathbf{u}}^{n+1}$ (note that the barotropic mode and the fluid thickness are also partly advanced with Δt again for the purpose of assisting the calculations):

$$\left[\widehat{\mathbf{u}}^{n+1}, \overline{\mathbf{G}}^n \right] = \text{Baroclinic_FEuler}(\mathbf{u}^n, \tilde{\mathbf{u}}^n, \zeta^n, h^n, \Delta t), \quad (17a)$$

$$\widehat{\mathbf{u}}^{n+1} = \overline{\mathbf{u}}^n - \Delta t (f\mathbf{k} \times \overline{\mathbf{u}}^n + g\nabla\zeta^n - \overline{\mathbf{G}}^n). \quad (17b)$$

$$\begin{cases} \widehat{h}_k^{n+1} = h_k^n + \Delta t \mathbf{T}_k^h(h^n, \mathbf{u}^n), \\ \widehat{\zeta}^{n+1} = \sum_{k=1}^L \widehat{h}_k^{n+1} - H, \\ \widehat{\mathbf{u}}_k^{n+1} = \widehat{\mathbf{u}}^{n+1} + \widehat{\mathbf{u}}_k^{n+1}. \end{cases} \quad (17c)$$

$$\begin{cases} \left[\widehat{\mathbf{u}}^{n+2}, \overline{\mathbf{G}}^{n+1} \right] = \text{Baroclinic_FEuler}(\widehat{\mathbf{u}}^{n+1}, \widehat{\mathbf{u}}^{n+1}, \widehat{\zeta}^{n+1}, \widehat{h}^{n+1}, \Delta t), \\ \widehat{\mathbf{u}}^{n+1/2} = \frac{3}{4}\tilde{\mathbf{u}}^n + \frac{1}{4}\widehat{\mathbf{u}}^{n+2}. \end{cases} \quad (18a)$$

$$\begin{cases} \widehat{\mathbf{u}}^{n+2} = \widehat{\mathbf{u}}^{n+1} - \Delta t (f\mathbf{k} \times \widehat{\mathbf{u}}^{n+1} + g\nabla\widehat{\zeta}^{n+1} - \overline{\mathbf{G}}^{n+1}), \\ \widehat{\mathbf{u}}^{n+1/2} = \frac{3}{4}\overline{\mathbf{u}}^n + \frac{1}{4}\widehat{\mathbf{u}}^{n+2}. \end{cases} \quad (18b)$$

$$\begin{cases} \widehat{h}_k^{n+2} = \widehat{h}_k^{n+1} + \Delta t \mathbf{T}_k^h(\widehat{h}^{n+1}, \widehat{\mathbf{u}}^{n+1}), \quad \widehat{h}_k^{n+1/2} = \frac{3}{4}h_k^n + \frac{1}{4}\widehat{h}_k^{n+2}, \\ \widehat{\zeta}^{n+1/2} = \sum_{k=1}^L \widehat{h}_k^{n+1/2} - H, \\ \widehat{\mathbf{u}}_k^{n+1/2} = \widehat{\mathbf{u}}^{n+1/2} + \widehat{\mathbf{u}}_k^{n+1/2}. \end{cases} \quad (18c)$$

$$\begin{cases} \left[\widehat{\mathbf{u}}^{n+3/2}, \overline{\mathbf{G}}^{n+1/2} \right] = \text{Baroclinic_FEuler}(\widehat{\mathbf{u}}^{n+1/2}, \widehat{\mathbf{u}}^{n+1/2}, \widehat{\zeta}^{n+1/2}, \widehat{h}^{n+1/2}, \Delta t), \\ \tilde{\mathbf{u}}^{n+1} = \frac{1}{3}\tilde{\mathbf{u}}^n + \frac{2}{3}\widehat{\mathbf{u}}^{n+3/2}. \end{cases} \quad (19a)$$

- **Step 2.** Advance the barotropic subsystem (7b) with the interpolated barotropic forcing $\text{Eval}_3(\overline{\mathbf{G}})$ (15) from t_n using SSPRK3 with the small time-step size $\Delta t/M$ to compute the correct barotropic velocity $\overline{\mathbf{u}}^{n+1}$:

$$\left[\overline{\mathbf{u}}^{n+1} \right] = \text{Barotropic_SSPRK3_Substepping}(\overline{\mathbf{u}}^n, \zeta^n, \overline{\mathbf{G}}^n, \overline{\mathbf{G}}^{n+1}, \overline{\mathbf{G}}^{n+1/2}, \Delta t, M). \quad (19b)$$

- **Step 3.** Combining the predicted barotropic and baroclinic velocities ($\tilde{\mathbf{u}}^{n+1}$ and $\overline{\mathbf{u}}^{n+1}$) to continue advancing the fluid thickness (left part from Step 1) to obtain h_k^{n+1} and then update

the SSH perturbation ζ^{n+1} :

$$\left\{ \begin{array}{l} \mathbf{u}_k^{n+1} = \bar{\mathbf{u}}^{n+1} + \tilde{\mathbf{u}}_k^{n+1}. \\ \hat{h}_k^{n+3/2} = \hat{h}_k^{n+1/2} + \Delta t \mathbf{T}_k^h \left(\hat{h}^{n+1/2}, \frac{1}{2}(\mathbf{u}_k^n + \mathbf{u}_k^{n+1}) \right), \\ h_k^{n+1} = \frac{1}{3}h_k^n + \frac{2}{3}\hat{h}_k^{n+3/2}, \\ \zeta^{n+1} = \sum_{k=1}^L h_k^{n+1} - H. \end{array} \right. \quad (19c)$$

The total cost of SSPRK3-SE per time step mainly consists of 3 times of forward-Euler baroclinic solve (i.e., $O(3LN)$) and M times of three forward-Euler barotropic solve (i.e., $O(3MN)$).

Remark 3.1. *In the above SSPRK2-SE or SSPRK3-SE schemes, the numerical stability of the baroclinic mode solve follows the SSPRK2 or SSPRK3 schemes with the time-step size Δt , while the stability of the barotropic mode solve follows that with the small time-step size $\Delta t/M$ due the corrections by substeppings.*

4. Temporal truncation error analysis

In this section, we analyze the temporal truncation errors of the proposed SSPRK-based multirate split-explicit schemes. Note that in the following analysis we only consider the semidiscrete-in-time case of the baroclinic-barotropic split system (7), i.e., there is no spatial discretization done to the system. It is also assumed that no vertical mixing is applied (i.e., Algorithm 1 is used) and the solutions always have sufficient smoothness as needed. To simplify the discussion, we first introduce the following notations:

$$\begin{aligned} \bar{\mathbf{G}}^* &= \begin{cases} \frac{1}{2}(\bar{\mathbf{G}}^n + \bar{\mathbf{G}}^{n+1}), & \text{for SSPRK2-SE,} \\ \frac{1}{6}\bar{\mathbf{G}}^n + \frac{1}{6}\bar{\mathbf{G}}^{n+1} + \frac{2}{3}\bar{\mathbf{G}}^{n+1/2}, & \text{for SSPRK3-SE,} \end{cases} \\ F^n &= f\mathbf{k} \times \bar{\mathbf{u}}^n + g\nabla\zeta^n - \bar{\mathbf{G}}^*, \\ P^n &= \nabla \cdot (\bar{\mathbf{u}}^n(\zeta^n + H)), \\ E^n &= f\mathbf{k} \times F^n + g\nabla P^n, \\ Q^n &= \nabla \cdot (\mathbf{u}^n P^n + (\zeta^n + H)F^n), \\ \eta^n &= f\mathbf{k} \times (f\mathbf{k} \times E^n + g\nabla Q^n) + g\nabla (\nabla \cdot (E^n(\zeta^n + H) + \bar{\mathbf{u}}^n Q^n + 2F^n P^n)), \\ \tau^n &= g\nabla (\nabla \cdot (F^n P^n)). \end{aligned}$$

First consider Algorithms 3 and 4 with regards to their accuracies.

Proposition 1. *Given*

$$[\bar{\mathbf{u}}^{n+1}] = \text{Barotropic_SSPRK2_Substepping} \left(\bar{\mathbf{u}}^n, \zeta^n, \bar{\mathbf{G}}^n, \bar{\mathbf{G}}^{n+1}, \Delta t, M \right),$$

then

$$\bar{\mathbf{u}}^{n+1} = \bar{\mathbf{u}}^n - \Delta t F^n + \frac{\Delta t^2}{2} E^n - \frac{M^2 - 1}{3M^2} \Delta t^3 (f\mathbf{k} \times E^n + g\nabla Q^n) + o(\Delta t^3). \quad (20)$$

Proof. Given $(\bar{\mathbf{u}}^{n+(j-1)/M}, \zeta^{n+(j-1)/M})$, after one substep in Algorithm 3, we have

$$\begin{cases} \bar{\mathbf{u}}^{n+j/M} = \bar{\mathbf{u}}^{n+(j-1)/M} - \frac{\Delta t}{M} F^{n+(j-1)/M} + \frac{\Delta t^2}{2M^2} E^{n+(j-1)/M}, \\ \zeta^{n+j/M} = \zeta^{n+(j-1)/M} - \frac{\Delta t}{M} P^{n+(j-1)/M} + \frac{\Delta t^2}{2M^2} Q^{n+(j-1)/M} - \frac{\Delta t^3}{2M^3} \nabla \cdot (F^{n+(j-1)/M} P^{n+(j-1)/M}). \end{cases} \quad (21)$$

By mathematical induction, we can obtain

$$\begin{cases} \bar{\mathbf{u}}^{n+j/M} = \bar{\mathbf{u}}^n - \frac{j\Delta t}{M} F^n + \frac{(j\Delta t)^2}{2M^2} E^n - \frac{j(j^2-1)}{3M^3} \Delta t^3 (f\mathbf{k} \times E^n + g\nabla Q^n) + o(\Delta t^3), \\ \zeta^{n+j/M} = \zeta^n - \frac{j\Delta t}{M} P^n + \frac{(j\Delta t)^2}{2M^2} Q^n + o(\Delta t^2). \end{cases} \quad (22)$$

Then (20) follows directly by setting $j = M$ in (22). \square

Proposition 2. *Given*

$$[\bar{\mathbf{u}}^{n+1}] = \text{Barotropic_SSPRK3_Substepping} \left(\bar{\mathbf{u}}^n, \zeta^n, \bar{\mathbf{G}}^n, \bar{\mathbf{G}}^{n+1}, \bar{\mathbf{G}}^{n+1/2}, \Delta t, M \right),$$

then

$$\bar{\mathbf{u}}^{n+1} = \bar{\mathbf{u}}^n - \Delta t F^n + \frac{\Delta t^2}{2} E^n - \frac{\Delta t^3}{6} (f\mathbf{k} \times E^n + g\nabla Q^n) + \frac{(M-1)(M^2+3)}{24M^3} \Delta t^4 \eta^n + \frac{\Delta t^4}{6M^3} \tau^n + o(\Delta t^4). \quad (23)$$

Proof. Given $(\bar{\mathbf{u}}^{n+(j-1)/M}, \zeta^{n+(j-1)/M})$, after one SSPRK3 substep in Algorithm 4 we have

$$\begin{aligned} \bar{\mathbf{u}}^{n+j/M} &= \bar{\mathbf{u}}^{n+(j-1)/M} - \frac{\Delta t}{M} F^{n+(j-1)/M} + \frac{\Delta t^2}{2M^2} E^{n+(j-1)/M} \\ &\quad - \frac{\Delta t^3}{6M^3} \left(f\mathbf{k} \times E^{n+(j-1)/M} + g\nabla Q^{n+(j-1)/M} \right) \\ &\quad + \frac{\Delta t^4}{6M^4} g\nabla (\nabla \cdot (F^{n+(j-1)/M} P^{n+(j-1)/M})), \\ \zeta^{n+j/M} &= \zeta^{n+(j-1)/M} - \frac{\Delta t}{M} P^{n+(j-1)/M} + \frac{\Delta t^2}{2M^2} Q^{n+(j-1)/M} \\ &\quad - \frac{\Delta t^3}{6M^3} \left(2\nabla \cdot (F^{n+(j-1)/M} P^{n+(j-1)/M}) \right) \\ &\quad + \nabla \cdot \left(E^{n+(j-1)/M} (\zeta^{n+(j-1)/M} + H) + \bar{\mathbf{u}}^{n+(j-1)/M} Q^{n+(j-1)/M} \right) \\ &\quad + o(\Delta t^3). \end{aligned} \quad (24)$$

By mathematical induction, we can easily obtain

$$\begin{aligned} \bar{\mathbf{u}}^{n+j/M} &= \bar{\mathbf{u}}^n - \frac{j\Delta t}{M} F^n + \frac{(j\Delta t)^2}{2M^2} E^n - \frac{j^3}{6M^3} \Delta t^3 (f\mathbf{k} \times E^n + g\nabla Q^n) \\ &\quad + \frac{(j-1)(j^3+3j)}{24M^4} \Delta t^4 \eta^n + \frac{j}{6M^4} \Delta t^4 \tau^n + o(\Delta t^4), \\ \zeta^{n+j/M} &= \zeta^n - \frac{j\Delta t}{M} P^n + \frac{(j\Delta t)^2}{2M^2} Q^n - \frac{(j\Delta t)^3}{6M^3} \nabla \cdot (E^n (\zeta^n + H) + \bar{\mathbf{u}}^n Q^n + 2F^n P^n) + o(\Delta t^3). \end{aligned} \quad (25)$$

Finally setting $j = M$ in (25) gives us (23). \square

Theorem 4.1. *The SSPRK2-SE scheme gives a third-order truncation error in time for solving the baroclinic-barotropic split system (7).*

Proof. The essential difference between the proposed SSPRK2-SE and the classical SSPRK2 is the calculations of the barotropic velocity and layer thickness at Steps 2 and 3. It is obvious that the time-stepping of the baroclinic velocity strictly follows the SSPRK2 scheme with the time-step size Δt . Therefore, the baroclinic velocity has third-order truncation error as guaranteed by the classic result for SSPRK2.

By taking the time derivative on Equation (7b), we have

$$\frac{\partial^2 \bar{\mathbf{u}}}{\partial t^2} = f\mathbf{k} \times (f\mathbf{k} \times \bar{\mathbf{u}} + g\nabla\zeta - \bar{\mathbf{G}}) + g\nabla(\nabla \cdot (\bar{\mathbf{u}}(\zeta + H))) + \frac{\partial \bar{\mathbf{G}}}{\partial t}. \quad (26)$$

According to Proposition 1, the barotropic velocity is given by

$$\begin{aligned} \bar{\mathbf{u}}^{n+1} &= \bar{\mathbf{u}}^n - \Delta t F^n + \frac{\Delta t^2}{2} E^n + o(\Delta t^2) \\ &= \bar{\mathbf{u}}^n - \Delta t \left(f\mathbf{k} \times \bar{\mathbf{u}}^n + g\nabla\zeta^n - \frac{1}{2} (\bar{\mathbf{G}}^n + \bar{\mathbf{G}}^{n+1}) \right) \\ &\quad + \frac{\Delta t^2}{2} \left(f\mathbf{k} \times \left(f\mathbf{k} \times \bar{\mathbf{u}}^n + g\nabla\zeta^n - \frac{1}{2} (\bar{\mathbf{G}}^n + \bar{\mathbf{G}}^{n+1}) \right) \right) \\ &\quad + \frac{\Delta t^2}{2} (g\nabla(\nabla \cdot (\bar{\mathbf{u}}^n(\zeta^n + H)))) + O(\Delta t^3). \end{aligned} \quad (27)$$

To identify the truncation error of the SSPRK2-SE scheme, we replace the numerical solutions by their exact counterparts, which yields

$$\begin{aligned} \bar{\mathbf{u}}(t_{n+1}) &= \bar{\mathbf{u}}(t_n) - \Delta t \left(f\mathbf{k} \times \bar{\mathbf{u}}(t_n) + g\nabla\zeta(t_n) - \frac{1}{2} (\bar{\mathbf{G}}(t_n) + \bar{\mathbf{G}}(t_{n+1})) \right) \\ &\quad + \frac{\Delta t^2}{2} \left(f\mathbf{k} \times \left(f\mathbf{k} \times \bar{\mathbf{u}}(t_n) + g\nabla\zeta(t_n) - \frac{1}{2} (\bar{\mathbf{G}}(t_n) + \bar{\mathbf{G}}(t_{n+1})) \right) \right) \\ &\quad + \frac{\Delta t^2}{2} (g\nabla(\nabla \cdot (\bar{\mathbf{u}}(t_n)(\zeta(t_n) + H)))) + O(\Delta t^3) \\ &= \bar{\mathbf{u}}(t_n) - \Delta t \left(f\mathbf{k} \times \bar{\mathbf{u}}(t_n) + g\nabla\zeta(t_n) - \bar{\mathbf{G}}(t_n) - \frac{\Delta t}{2} \frac{\partial \bar{\mathbf{G}}(t_n)}{\partial t} \right) \\ &\quad + \frac{\Delta t^2}{2} (f\mathbf{k} \times (f\mathbf{k} \times \bar{\mathbf{u}}(t_n) + g\nabla\zeta(t_n) - \bar{\mathbf{G}}(t_n))) \\ &\quad + \frac{\Delta t^2}{2} (g\nabla(\nabla \cdot (\bar{\mathbf{u}}(t_n)(\zeta(t_n) + H)))) + O(\Delta t^3) \\ &= \bar{\mathbf{u}}(t_n) - \Delta t (f\mathbf{k} \times \bar{\mathbf{u}}(t_n) + g\nabla\zeta(t_n) - \bar{\mathbf{G}}(t_n)) + \frac{\Delta t^2}{2} \frac{\partial^2 \bar{\mathbf{u}}(t_n)}{\partial t^2} + O(\Delta t^3), \end{aligned} \quad (28)$$

which implies the barotropic velocity has a third-order truncation error. For the layer thickness h , we can rewrite its formula in a compact way, that is

$$h^{n+1} = h^n - \frac{\Delta t}{2} \left(\mathbf{T}_k^h(h^n, \mathbf{u}^n) + \mathbf{T}_k^h(\hat{h}^{n+1}, \mathbf{u}^{n+1}) \right). \quad (29)$$

Notice that here we have used the second order accurate solution \mathbf{u}^{n+1} instead of the first order accurate velocity $\hat{\mathbf{u}}^{n+1}$. In addition, the error between \mathbf{u}^{n+1} and $\hat{\mathbf{u}}^{n+1}$ is $O(\Delta t^2)$. Based on the

classic results of the SSPRK2 scheme, we know that

$$\tilde{h}^{n+1} = h^n - \frac{\Delta t}{2} \left(\mathbf{T}_k^h(h^n, \mathbf{u}^n) + \mathbf{T}_k^h(\hat{h}^{n+1}, \hat{\mathbf{u}}^{n+1}) \right) \quad (30)$$

gives us a third order truncation error in time, i.e., $|\tilde{h}^{n+1} - h(t_{n+1})| = O(\Delta t^3)$. Furthermore,

$$|h^{n+1} - \tilde{h}^{n+1}| = \left| \frac{\Delta t}{2} \left(\mathbf{T}_k^h(\hat{h}^{n+1}, \mathbf{u}^{n+1}) - \mathbf{T}_k^h(\hat{h}^{n+1}, \hat{\mathbf{u}}^{n+1}) \right) \right| = O(\Delta t^3), \quad (31)$$

thus it holds that h^{n+1} also has a third-order truncation error in time. \square

By using similar analysis with Proposition 2, we also can prove the following result.

Theorem 4.2. *The SSPRK3-SE scheme gives a fourth-order truncation error in time for solving the baroclinic-barotropic system (7).*

Remark 4.3. *In MPAS-Ocean, the baroclinic-barotropic split system (7) is discretized in space by the TRiSK scheme (a specially-designed finite volume approximation) on unstructured, locally orthogonal dual meshes [28, 45, 29] to ensure many physical properties of the space-continuous system in the spatially discrete setting, such as the conservations of mass, total energy, and potential vorticity. Our numerical experiments will be based on the MPAS-Ocean platform and use the same spatial discretization. The inconsistency caused by the determination of the SSH perturbation ζ after discretizing the baroclinic-barotropic split system in space (see Remark 2.2) is often referred to as the mode-splitting error in the literature. As seen from (7), $g\nabla\zeta$ directly contributes to the flux of $\bar{\mathbf{u}}$, and thus when a fully discrete (in both space and time) system is considered, the inconsistency of ζ will introduce an error of $C_{SE}(\Delta\mathbf{x})\Delta t$ to the approximation of $\bar{\mathbf{u}}$, where the constant $C_{SE}(\Delta\mathbf{x})$ is dependent on the spatial mesh size $\Delta\mathbf{x}$. This error might dominate the overall error of the scheme and degrade the accuracy order of time-stepping schemes when $C_{SE}(\Delta\mathbf{x})$ is large and the time-step size Δt is small.*

5. Numerical experiments

We implement the proposed SSPRK-based multirate explicit time-stepping schemes (SSPRK2-SE and SSPRK3-SE) within the framework of MPAS-Ocean (using its built-in subroutines). To investigate their accuracy and performance, we use two benchmark test cases from the MPAS-Ocean platform (Version 7.0) [27]. In these two cases, the bottom drag is considered as a bottom boundary condition:

$$\lim_{z \rightarrow z_{\text{bot}}} \nu_v \frac{\partial \mathbf{u}}{\partial z} = c_{\text{drag}} |\mathbf{u}| \mathbf{u}, \quad (32)$$

where $|\mathbf{u}|$ denotes the magnitude of the velocity, c_{drag} is the bottom drag coefficient, and z_{bot} is the z-location of the ocean bottom. In the following numerical experiments, if the results are obtained with the vertical mixing, we will call Algorithm 2 (“Baroclinic.FEuler.Mixing”) instead of Algorithm 1 (“Baroclinic.FEuler”) to advance the baroclinic mode in the proposed SSPRK2-SE and SSPRK3-SE schemes. The time-step size used for the barotropic substepping (Algorithm 3 or 4) in the last stage is denoted by $\Delta_{\text{btr}} = \Delta t/M$. In order to measure the accuracy, the relative l_2 error is used for evaluation of the velocity \mathbf{u}_1 (i.e. the surface velocity) and the layer thickness h_1 (i.e., the top layer thickness) at the terminal time T :

$$\frac{\|\mathbf{u}_1^t - \mathbf{u}_1^r\|_2}{\|\mathbf{u}_1^r\|_2} \quad \text{and} \quad \frac{\|h_1^t - h_1^r\|_2}{\|h_1^r\|_2},$$

where \mathbf{u}_1^r and h_1^r are the reference values, \mathbf{u}_1^t and h_1^t are the testing values, and $\|\cdot\|_2$ is the vector l_2 -norm. All numerical experiments are performed on the cluster ‘‘Cori’’ at the National Energy Research Scientific Computing Center (NERSC). In particular, we run our codes on the ‘‘Haswell’’ processor nodes for which each node has two 16-core Intel Xeon ‘‘Haswell’’ (E5-2698 v3, 2.3 GHz) processors and 128 GB DDR4 2133 MHz memory.

5.1. The baroclinic eddies test case for the primitive equations with twenty layers

We first consider an ideal test case, namely the baroclinic eddies test case [21, 27], for the primitive equations with 20 vertical layers provided by the MPAS-Ocean platform imported from [46]. The domain consists of a horizontally periodic channel of latitudinal extent 500 km and longitudinal extent 160 km, with a flat bottom of 1 km vertical depth. The channel is on a f-plane [6] with the Coriolis parameter $f = 1.2 \times 10^{-4} \text{ s}^{-1}$, where s denotes seconds. The initial temperature decreases downward in the meridional direction. A cosine shaped temperature perturbation with a wavelength of 120 km in the zonal direction is used to instigate the baroclinic instability. The horizontal domain is partitioned by a 10-km-resolution SCVT mesh [47] such that each layer contains 3,920 cells, 11,840 edges, and 7,920 vertices. The horizontal viscosity is given as $\nu_h = 10$ and the vertical one as $\nu_v = 1.0\text{E-}4$.

We first test the temporal convergence order of the current dynamical core (the MPAS-SE scheme) in MPAS-Ocean. Vertical mixing is always applied by default in the MPAS-SE scheme in its current implementation. We set the terminal time at $T = 4096 \text{ s}$ and choose the referential values generated by itself with $\Delta t = \Delta_{\text{btr}} t = 0.25 \text{ s}$ (i.e., $M = 1$). We comment out the update of the tracers because in this test we are only interested in the ocean dynamics. The relative l_2 errors in the velocity and layer thickness approximations are reported in Table 2, which shows that the MPAS-SE scheme explodes when $\Delta t = 128 \text{ s}$ and the temporal convergence rates are only less than or close to one for both variables.

$\Delta t - \Delta_{\text{btr}} t$ (s)	Velocity		Layer thickness	
	Error	Rate	Error	Rate
128-128	N/A	-	N/A	-
64-64	2.35E-02	-	1.46E-05	-
32-32	2.07E-02	0.19	1.30E-05	0.18
16-16	1.64E-02	0.34	9.91E-06	0.39
08-08	1.19E-02	0.46	6.81E-06	0.54
04-04	7.99E-03	0.57	4.33E-06	0.65
02-02	4.89E-03	0.71	2.53E-06	0.78
01-01	2.58E-03	0.92	1.29E-06	0.97

Table 2: Relative l_2 errors and convergence rates of \mathbf{u}_1 and h_1 for the baroclinic eddies test case produced by the MPAS-SE scheme.

Next, we test the proposed SSPRK2-SE and SSPRK3-SE schemes in terms of accuracy for $M = 1, 2, 4,$ and 8 . We compute the relative l_2 errors of the velocity and layer thickness approximations at $T = 4096 \text{ s}$ with the reference value generated by using the SSPRK3-SE scheme without vertical mixing with $\Delta t = \Delta_{\text{btr}} t = 0.25 \text{ s}$. The results produced by the schemes without vertical mixing are given in Table 3 and those by the schemes with vertical mixing in Table 4. For SSPRK2-SE scheme, it is observed that the second-order temporal convergence is achieved for both the velocity and fluid thickness, with or without vertical mixing, for all choices of M as the time-step sizes are uniformly refined. For the SSPRK2-SE3 scheme, the third-order temporal convergence is achieved for the fluid thickness, with or without vertical mixing, for all choices of M , whereas the third-order

temporal convergence for velocity is obtained until the error is reduced to the magnitude of $1.0\text{E-}6$. We believe a possible reason is an inconsistency error in velocity due to the mode splitting begins to take some effect at that level and degrades the temporal convergence whereas that for the layer thickness is much smaller. We also observe that the SSPRK3-SE scheme always yields smaller errors than the SSPRK2-SE schemes for the same time-step sizes. Additionally, we note that in this test case the vertical mixing does not affect the accuracies, i.e., the errors generated by such processes are negligible.

M	$\Delta t - \Delta_{\text{btr}} t$	Velocity				Layer thickness			
		SSPRK2-SE		SSPRK3-SE		SSPRK2-SE		SSPRK3-SE	
		Error	Rate	Error	Rate	Error	Rate	Error	Rate
1	64-64	1.16E-02	-	3.93E-03	-	4.93E-06	-	1.81E-06	-
	32-32	5.41E-03	1.10	1.11E-03	1.83	2.35E-06	1.07	4.99E-07	1.86
	16-16	1.47E-03	1.89	1.60E-04	2.79	6.28E-07	1.90	7.29E-08	2.77
	08-08	3.63E-04	2.01	2.04E-05	2.98	1.57E-07	2.00	9.31E-09	2.97
	04-04	9.04E-05	2.00	2.57E-06	2.98	3.93E-08	2.00	1.17E-09	3.00
	02-02	2.26E-05	2.00	3.65E-07	2.82	9.81E-09	2.00	1.46E-10	3.00
2	64-32	5.82E-03	-	3.42E-03	-	2.57E-06	-	1.70E-06	-
	32-16	2.58E-03	1.17	4.06E-04	3.07	1.15E-06	1.15	1.80E-07	3.24
	16-08	7.57E-04	1.77	4.65E-05	3.13	3.42E-07	1.75	2.10E-08	3.09
	08-04	1.94E-04	1.97	5.75E-06	3.02	8.58E-08	1.99	2.60E-09	3.02
	04-02	4.86E-05	1.99	8.07E-07	2.83	2.13E-08	2.01	3.25E-10	3.00
	02-01	1.22E-05	1.99	2.01E-07	2.00	5.32E-09	2.00	4.09E-11	2.99
4	128-32	5.75E-01	-	1.26E-02	-	2.80E-03	-	6.19E-06	-
	64-16	8.08E-03	6.15	6.48E-03	0.96	3.40E-06	9.68	3.15E-06	0.98
	32-08	3.99E-03	1.02	6.30E-04	3.36	1.74E-06	0.97	2.79E-07	3.49
	16-04	1.27E-03	1.65	7.24E-05	3.12	5.68E-07	1.61	3.29E-08	3.09
	08-02	3.31E-04	1.94	8.96E-06	3.01	1.46E-07	1.96	4.08E-09	3.01
	04-01	8.32E-05	1.99	1.18E-06	2.93	3.64E-08	2.00	5.11E-10	3.00
8	128-16	1.46E-02	-	1.38E-02	-	6.69E-06	-	6.88E-06	-
	64-08	8.69E-03	0.75	7.04E-03	0.97	3.63E-06	0.88	3.39E-06	1.02
	32-04	4.34E-03	1.00	6.59E-04	3.42	1.89E-06	0.94	2.92E-07	3.53
	16-02	1.40E-03	1.63	7.56E-05	3.12	6.25E-07	1.59	3.43E-08	3.09
	08-01	3.65E-04	1.94	9.36E-06	3.01	1.61E-07	1.96	4.27E-09	3.01
	04-0.5	9.18E-05	1.99	1.23E-06	2.93	4.02E-08	2.00	5.34E-10	3.00

Table 3: Relative l_2 errors and convergence rates in \mathbf{u}_1 and h_1 for the baroclinic eddies test case produced by the SSPRK-based multirate explicit time-stepping schemes without vertical mixing.

Next, we fix $\Delta t = 64$ s, $M = 4$ and perform a 20 day-long simulations for the baroclinic eddies test case with different bottom drag coefficients using the SSPRK2-SE scheme without vertical mixing. The temperature tracer equation is also added by adopting the treatment of tracers from MPAS-Ocean. Snapshots of the surface temperature on days 5, 10, 15 and 20 are shown in Figure 1, where the top row is associated with the case of $c_{\text{drag}} = 0.01$ and the bottom row with $c_{\text{drag}} = 0.001$. It is observed that for the weaker bottom drag, the eddies escape further away from the interface as is expected. The results obtained by the SSPRK2-SE scheme with vertical mixing are almost identical so they are not shown. In addition, we also perform the same simulation using the MPAS-SE scheme and plot the evolutions of the average absolute difference between the simulated surface temperatures produced by SSPRK2-SE and MPAS-SE in Figure 2. We observe that the differences gradually become larger with increasing time for both bottom drag choices. Because the eddies travel faster for the smaller bottom drag case, the choice $c_{\text{drag}} = 0.001$ results in even

M	$\Delta t - \Delta_{\text{btr}} t$	Velocity				Layer thickness			
		SSPRK2-SE		SSPRK3-SE		SSPRK2-SE		SSPRK3-SE	
		Error	Rate	Error	Rate	Error	Rate	Error	Rate
1	64-64	1.16E-02	-	3.93E-03	-	4.93E-06	-	1.81E-06	-
	32-32	5.42E-03	1.10	1.11E-03	1.83	2.35E-06	1.07	4.99E-07	1.86
	16-16	1.47E-03	1.89	1.60E-04	2.79	6.28E-07	1.90	7.29E-08	2.77
	08-08	3.63E-04	2.01	2.04E-05	2.98	1.57E-07	2.00	9.31E-09	2.97
	04-04	9.05E-05	2.00	2.63E-06	2.95	3.93E-08	2.00	1.17E-09	3.00
	02-02	2.27E-05	2.00	4.54E-07	2.54	9.81E-09	2.00	1.46E-10	3.00
2	64-32	5.81E-03	-	3.42E-03	-	2.57E-06	-	1.70E-06	-
	32-16	2.58E-03	1.17	4.06E-04	3.07	1.15E-06	1.15	1.80E-07	3.24
	16-08	7.57E-04	1.77	4.66E-05	3.12	3.42E-07	1.75	2.10E-08	3.09
	08-04	1.93E-04	1.97	5.87E-06	2.99	8.58E-08	1.99	2.60E-09	3.02
	04-02	4.85E-05	2.00	9.94E-07	2.56	2.13E-08	2.01	3.26E-10	2.99
	02-01	1.22E-05	2.00	3.37E-07	1.56	5.32E-09	2.00	4.34E-11	2.91
4	128-32	5.78E-01	-	1.26E-02	-	2.80E-03	-	6.19E-06	-
	64-16	8.08E-03	6.16	6.48E-03	0.96	3.40E-06	9.69	3.15E-06	0.98
	32-08	3.99E-03	1.02	6.30E-04	3.36	1.74E-06	0.97	2.79E-07	3.49
	16-04	1.27E-03	1.65	7.24E-05	3.12	5.68E-07	1.61	3.29E-08	3.09
	08-02	3.31E-04	1.94	9.04E-06	3.00	1.46E-07	1.96	4.08E-09	3.01
	04-01	8.31E-05	1.99	1.31E-06	2.78	3.64E-08	2.00	5.12E-10	3.00
8	128-16	1.46E-02	-	1.38E-02	-	6.69E-06	-	6.88E-06	-
	64-08	8.68E-03	0.75	7.04E-03	0.97	3.63E-06	0.88	3.39E-06	1.02
	32-04	4.34E-03	1.00	6.58E-04	3.42	1.89E-06	0.94	2.92E-07	3.53
	16-02	1.40E-03	1.63	7.57E-05	3.12	6.25E-07	1.59	3.43E-08	3.09
	08-01	3.65E-04	1.94	9.44E-06	3.00	1.61E-07	1.96	4.27E-09	3.01
	04-0.5	9.18E-05	1.99	1.36E-06	2.80	4.02E-08	2.00	5.35E-10	3.00

Table 4: Relative l_2 errors and convergence rates in \mathbf{u}_1 and h_1 for the baroclinic eddies test case produced by the SSPRK-based multirate explicit time-stepping schemes with vertical mixing.

larger differences between the SSPRK2-SE and MPAS-SE schemes compared to that for the choice $c_{\text{drag}} = 0.01$ which is again as expected.

5.2. The global ocean test case for the primitive equations with one hundred layers

Next, we consider a test case having a global real-world ocean configuration from the MPAS-Ocean platform. The horizontal SCVT mesh, denoted as ‘‘QU240’’, is quasi-uniform over the globe, with cell widths of 240 km. There are 100 layers and each of them contains 7,234 cells, 22,736 edges, and 15,459 vertices. As mentioned in Remark 2.1, the horizontal biharmonic operator with the coefficient $\nu_h = 2.0\text{E}14$ is applied as the hyperviscosity. In this test case, the bottom drag coefficient is $c_{\text{drag}} = 1.0\text{E}-3$ and the vertical viscosity is $\nu_v = 1.0\text{E}-4$. The initial temperature and salinity values at the ocean surface are shown in Figure 3.

We investigate the temporal accuracy of the proposed schemes by setting the terminal time to $T = 4096$ s and varying M from 1, 2, 4, 8 to 16. We again compute the relative l_2 errors of the velocity and layer thickness at $T = 4096$ s with the reference value generated by using the SSPRK3-SE scheme without vertical mixing with $\Delta t = \Delta_{\text{btr}} t = 1$ s. The numerical results are presented in Tables 5 and 6. Without vertical mixing, the SSPRK2-SE scheme can achieve second order convergence when Δt is relatively large, but the order degrades when the velocity error becomes smaller than about the magnitude of $1.0\text{E}-5$ and the layer thickness error is lower than about the magnitude of $1.0\text{E}-8$ due to the inconsistency errors caused by the mode splitting. The convergence

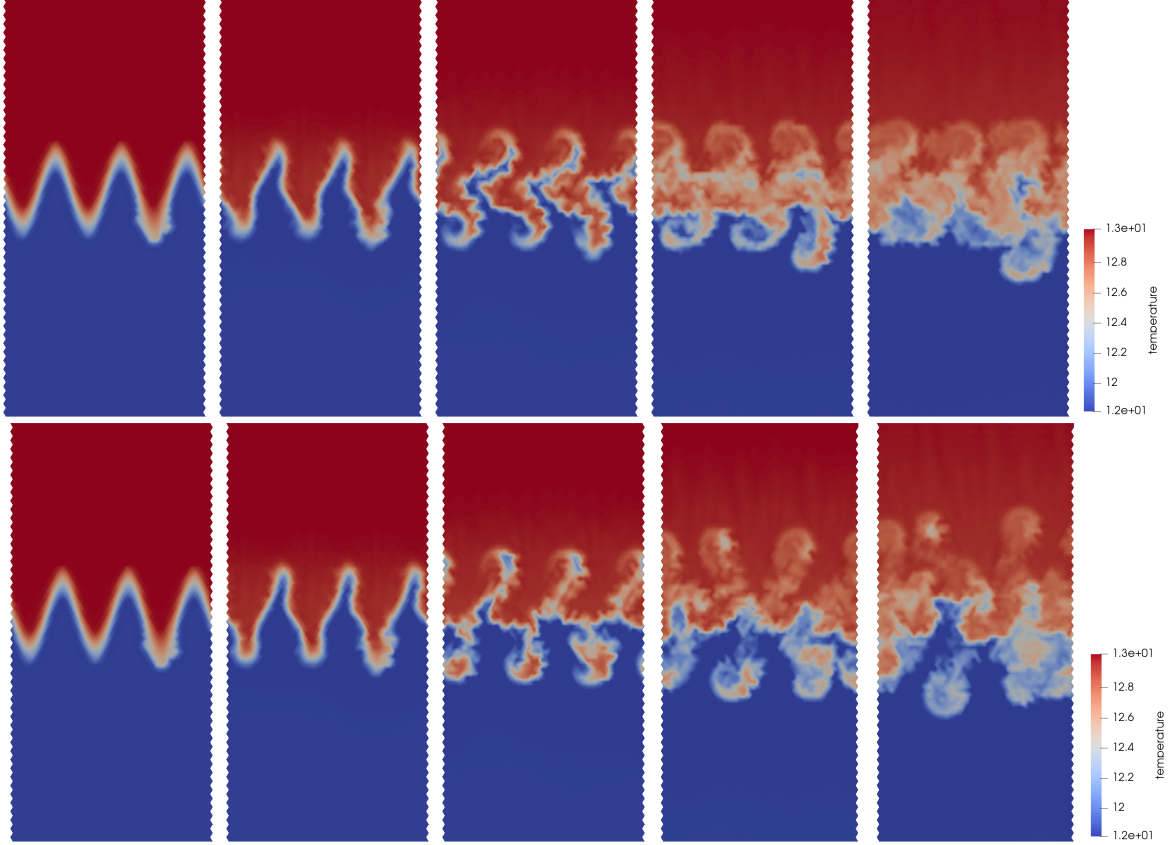


Figure 1: Simulated surface temperatures by using the SSPRK2-SE scheme (without vertical mixing) with $\Delta t = 64$ s, $M = 4$ for the baroclinic eddies test case. From left to right are the results at the initial time and Day 5, 10, 15 and 20. Top: $c_{\text{drag}} = 0.01$; bottom: $c_{\text{drag}} = 0.001$.

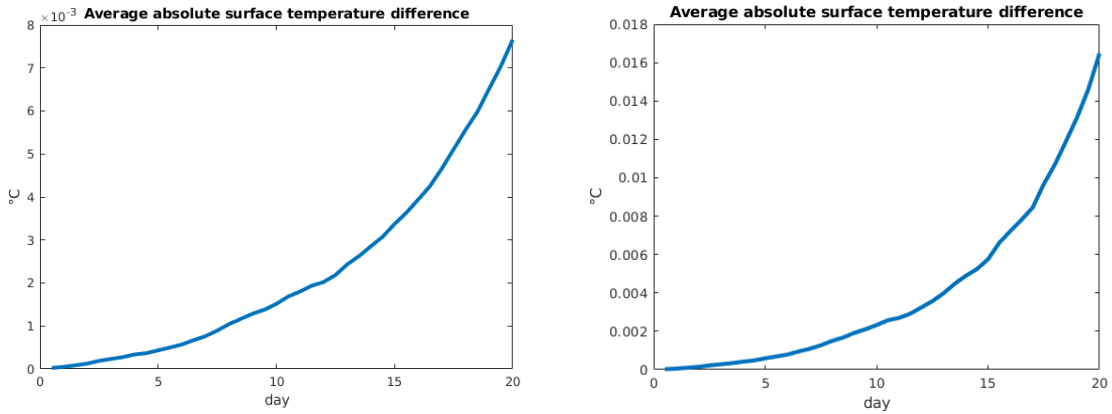


Figure 2: Evolutions of the average absolute differences between the simulated surface temperatures produced by using the SSPRK2-SE and MPAS-SE schemes with $\Delta t = 64$ s and $M = 4$. Left: $c_{\text{drag}} = 0.01$; right: $c_{\text{drag}} = 0.001$.

rates for the SSPRK3-SE scheme are even more affected by the inconsistency errors. Specifically, the error emanates from two causes: one is from the numerical scheme itself, $C\Delta t^3$, where C is independent of Δt and the mesh size $\Delta \mathbf{x}$, and the other one is from the splitting inconsistency, $C_{\text{SE}}(\Delta \mathbf{x})\Delta t$. When Δt is small and $\Delta \mathbf{x}$ is large, $C_{\text{SE}}(\Delta \mathbf{x})\Delta t$ may easily dominate over $C\Delta t^3$ and thus the convergence order is reduced to first order as predicted. On the other hand, the SSPRK3-

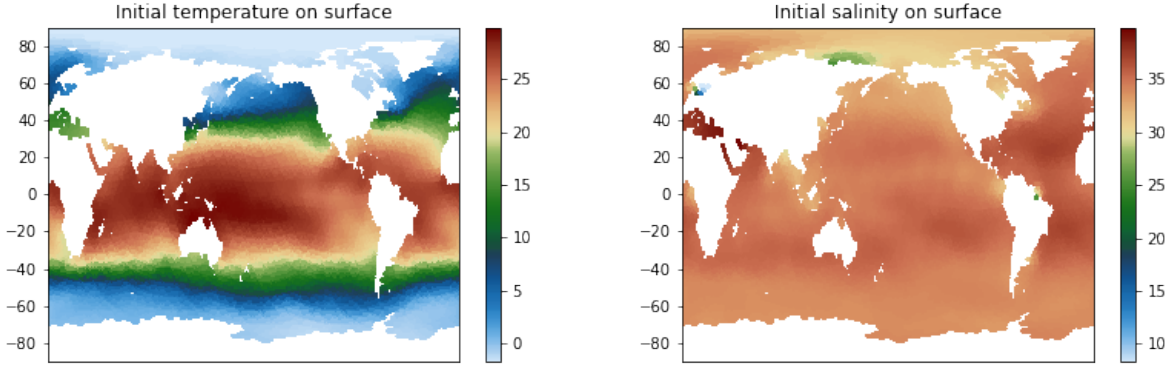


Figure 3: The initial temperature and salinity of the ocean surface for the global ocean test case.

SE scheme again yields smaller errors than the SSPRK2-SE schemes under the same time-step sizes, which makes the SSPRK3-SE a probably more favorable choice in practice.

M	$\Delta t - \Delta_{\text{btr}t}$	Velocity				Layer thickness			
		SSPRK2-SE		SSPRK3-SE		SSPRK2-SE		SSPRK3-SE	
		Error	Rate	Error	Rate	Error	Rate	Error	Rate
1	1024-1024	4.16E-03	-	3.95E-04	-	2.05E-06	-	3.80E-07	-
	512-512	5.49E-04	2.92	4.20E-05	3.23	2.98E-07	2.79	8.91E-08	2.09
	256-256	1.38E-04	1.99	1.34E-05	1.65	8.61E-08	1.79	4.32E-08	1.05
	128-128	3.60E-05	1.94	7.12E-06	0.91	3.03E-08	1.51	2.21E-08	0.96
	64-64	1.01E-05	1.84	3.62E-06	0.98	1.27E-08	1.26	1.11E-08	1.00
2	1024-512	1.91E-03	-	1.55E-04	-	7.53E-07	-	2.62E-07	-
	512-256	4.73E-04	2.01	3.93E-05	1.98	1.67E-07	2.18	9.17E-08	1.51
	256-128	1.20E-04	1.98	1.62E-05	1.28	5.05E-08	1.72	4.48E-08	1.03
	128-64	3.14E-05	1.93	7.56E-06	1.10	2.18E-08	1.21	2.24E-08	1.00
	64-32	8.83E-06	1.83	3.68E-06	1.04	1.08E-08	1.02	1.11E-08	1.01
4	1024-256	1.93E-03	-	1.77E-04	-	1.02E-06	-	2.89E-07	-
	512-128	4.84E-04	2.00	4.44E-05	1.99	2.50E-07	2.03	9.47E-08	1.61
	256-64	1.23E-04	1.98	1.67E-05	1.41	6.71E-08	1.90	4.51E-08	1.07
	128-32	3.19E-05	1.94	7.63E-06	1.13	2.38E-08	1.50	2.24E-08	1.01
	64-16	8.88E-06	1.85	3.68E-06	1.05	1.08E-08	1.13	1.11E-08	1.01
8	1024-128	1.94E-03	-	1.80E-04	-	1.08E-06	-	2.92E-07	-
	512-64	4.88E-04	1.99	4.51E-05	2.00	2.71E-07	2.00	9.51E-08	1.62
	256-32	1.24E-04	1.98	1.68E-05	1.43	7.19E-08	1.91	4.51E-08	1.08
	128-16	3.21E-05	1.94	7.63E-06	1.14	2.45E-08	1.56	2.24E-08	1.01
	64-08	8.91E-06	1.85	3.68E-06	1.05	1.09E-08	1.17	1.11E-08	1.01
16	1024-64	1.94E-03	-	1.81E-04	-	1.10E-06	-	2.92E-07	-
	512-32	4.89E-04	1.99	4.52E-05	2.00	2.76E-07	1.99	9.51E-08	1.62
	256-16	1.24E-04	1.98	1.68E-05	1.43	7.32E-08	1.92	4.51E-08	1.08
	128-08	3.22E-05	1.95	7.63E-06	1.14	2.46E-08	1.57	2.24E-08	1.01
	64-04	8.92E-06	1.85	3.68E-06	1.05	1.09E-08	1.18	1.11E-08	1.01

Table 5: Relative l_2 errors and convergence rates in \mathbf{u}_1 and h_1 for the global ocean test case produced by the proposed SSPRK-based multirate explicit time-stepping schemes without vertical mixing.

In this test case, the vertical mesh size is much smaller than the horizontal mesh width. When vertical mixing is applied, the accuracies of velocity for both the SSPRK2-SE and SSPRK3-SE

M	$\Delta t - \Delta_{\text{btrt}}$	Velocity				Layer thickness			
		SSPRK2-SE		SSPRK3-SE		SSPRK2-SE		SSPRK3-SE	
		Error	Rate	Error	Rate	Error	Rate	Error	Rate
1	1024-1024	3.12E-02	-	3.22E-02	-	2.06E-06	-	3.80E-07	-
	512-512	1.63E-02	0.94	1.66E-02	0.96	3.11E-07	2.73	8.92E-08	2.09
	256-256	8.32E-03	0.97	8.39E-03	0.98	9.77E-08	1.67	4.32E-08	1.05
	128-128	4.19E-03	0.99	4.21E-03	0.99	3.81E-08	1.36	2.21E-08	0.96
	64-64	2.09E-03	1.00	2.10E-03	1.01	1.71E-08	1.15	1.11E-08	1.00
2	1024-512	3.10E-02	-	3.22E-02	-	7.85E-07	-	2.61E-07	-
	512-256	1.63E-02	0.93	1.66E-02	0.96	1.96E-07	2.00	9.15E-08	1.51
	256-128	8.31E-03	0.97	8.39E-03	0.98	7.05E-08	1.48	4.48E-08	1.03
	128-64	4.19E-03	0.99	4.21E-03	0.99	3.24E-08	1.12	2.24E-08	1.00
	64-32	2.09E-03	1.00	2.10E-03	1.01	1.59E-08	1.02	1.11E-08	1.01
4	1024-256	3.10E-02	-	3.22E-02	-	1.05E-06	-	2.88E-07	-
	512-128	1.63E-02	0.93	1.66E-02	0.96	2.72E-07	1.95	9.45E-08	1.61
	256-64	8.31E-03	0.97	8.39E-03	0.98	8.37E-08	1.70	4.51E-08	1.07
	128-32	4.19E-03	0.99	4.21E-03	0.99	3.38E-08	1.31	2.24E-08	1.01
	64-16	2.09E-03	1.00	2.10E-03	1.01	1.60E-08	1.08	1.11E-08	1.01
8	1024-128	3.10E-02	-	3.22E-02	-	1.11E-06	-	2.91E-07	-
	512-64	1.62E-02	0.93	1.66E-02	0.96	2.91E-07	1.93	9.49E-08	1.62
	256-32	8.31E-03	0.97	8.39E-03	0.98	8.77E-08	1.73	4.51E-08	1.07
	128-16	4.19E-03	0.99	4.21E-03	0.99	3.43E-08	1.35	2.24E-08	1.01
	64-08	2.09E-03	1.00	2.10E-03	1.01	1.61E-08	1.10	1.11E-08	1.01
16	1024-64	3.10E-02	-	3.22E-02	-	1.12E-06	-	2.91E-07	-
	512-32	1.62E-02	0.93	1.66E-02	0.96	2.96E-07	1.92	9.50E-08	1.62
	256-16	8.31E-03	0.97	8.39E-03	0.98	8.87E-08	1.74	4.51E-08	1.07
	128-08	4.19E-03	0.99	4.21E-03	0.99	3.45E-08	1.36	2.24E-08	1.01
	64-04	2.09E-03	1.00	2.10E-03	1.01	1.61E-08	1.10	1.11E-08	1.01

Table 6: Relative l_2 errors and convergence rates in \mathbf{u}_1 and h_1 for the global ocean test case produced by the proposed SSPRK-based multirate explicit time-stepping schemes with vertical mixing.

schemes are both only the first order from the beginning due to strong effect of the first-order operator splitting errors (by vertical mixing) as shown in Table 6. For the layer thickness, the SSPRK2-SE scheme still can remain close to the second-order convergence when the errors are above the threshold magnitude of $1.0\text{E-}7$; the convergence of the SSPRK3-SE scheme quickly drop to the first order. This is partly due to the velocity affecting the layer thickness through the flux term, which always combines with an extra Δt ; thus the convergence rate of the fluid thickness could drop slower.

By adopting the treatment of tracers from MPAS-Ocean, the simulation with the final time $T = 20$ days is also carried out by using the SSPRK3-SE scheme (with vertical mixing) with $\Delta t = 256$ s and $M = 16$. The surface temperature and salinity increments on day 5, 10, 15, and 20 are shown in Figures 4 and 5. MPAS-Analysis [48] and SciVisColor Colormaps [49] are used to generate these figures. Besides, we also compare them with those produced by the MPAS-SE scheme in Figure 6. We observe that both of the differences in the temperatures and salinities gradually become larger during the first 10 days, but then start to decrease slowly with small oscillations during the next 10 days.

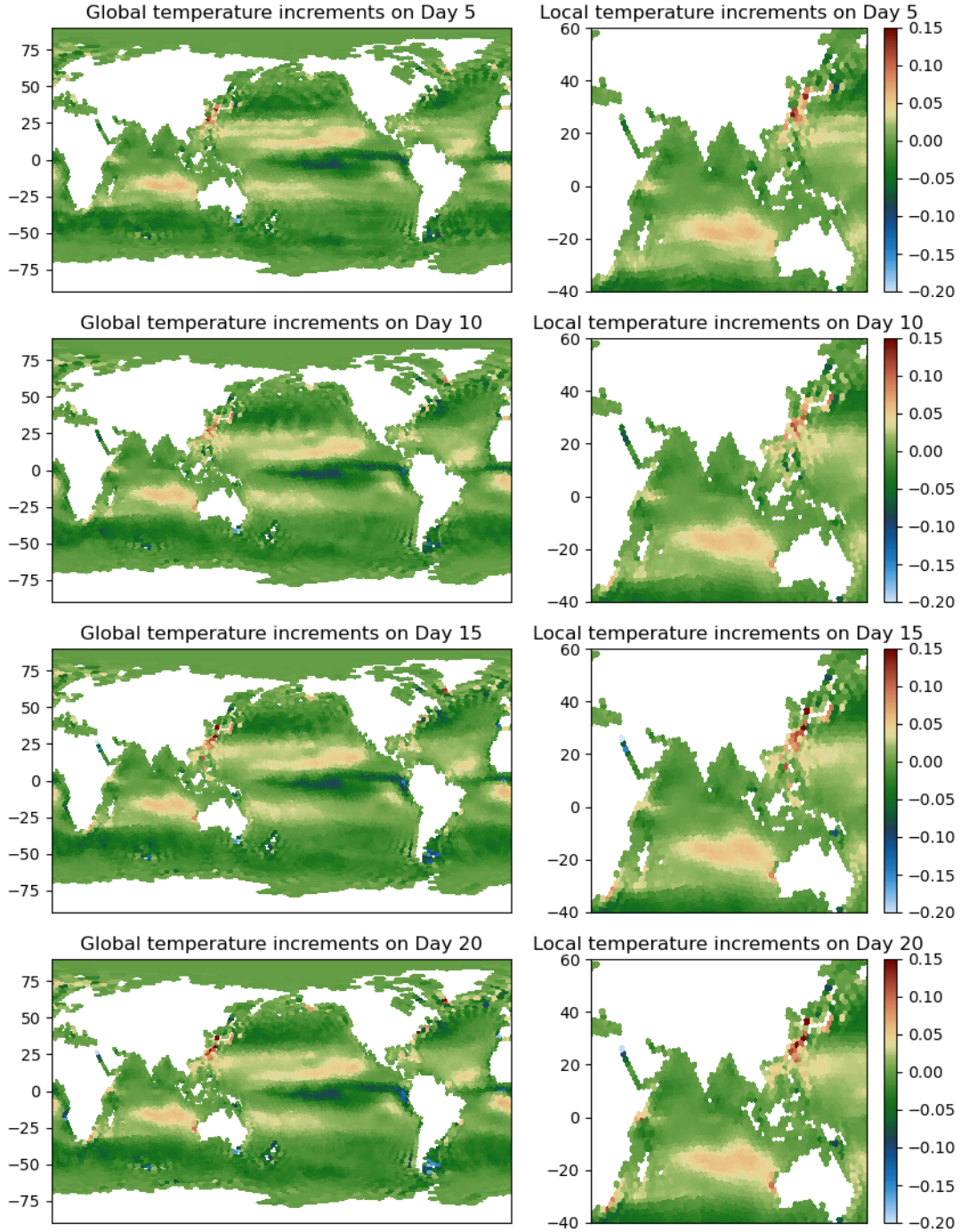


Figure 4: Simulated temperature increments using the SSPRK3-SE scheme with $\Delta t = 256$ s and $M = 16$ for the global ocean test case. From top to bottom are the results for Day 5, 10, 15, and 20. The left ones are the global temperature increments, and the right ones are for the local area at latitude from 40°S to 60°N , and longitude extending east-ward between 20°E and 160°E .

5.3. Parallel performance

We finish by testing the parallel performance of the proposed SSPRK2-SE and SSPRK3-SE schemes using the global ocean test case. Following the MAS-Ocean framework, the domain de-

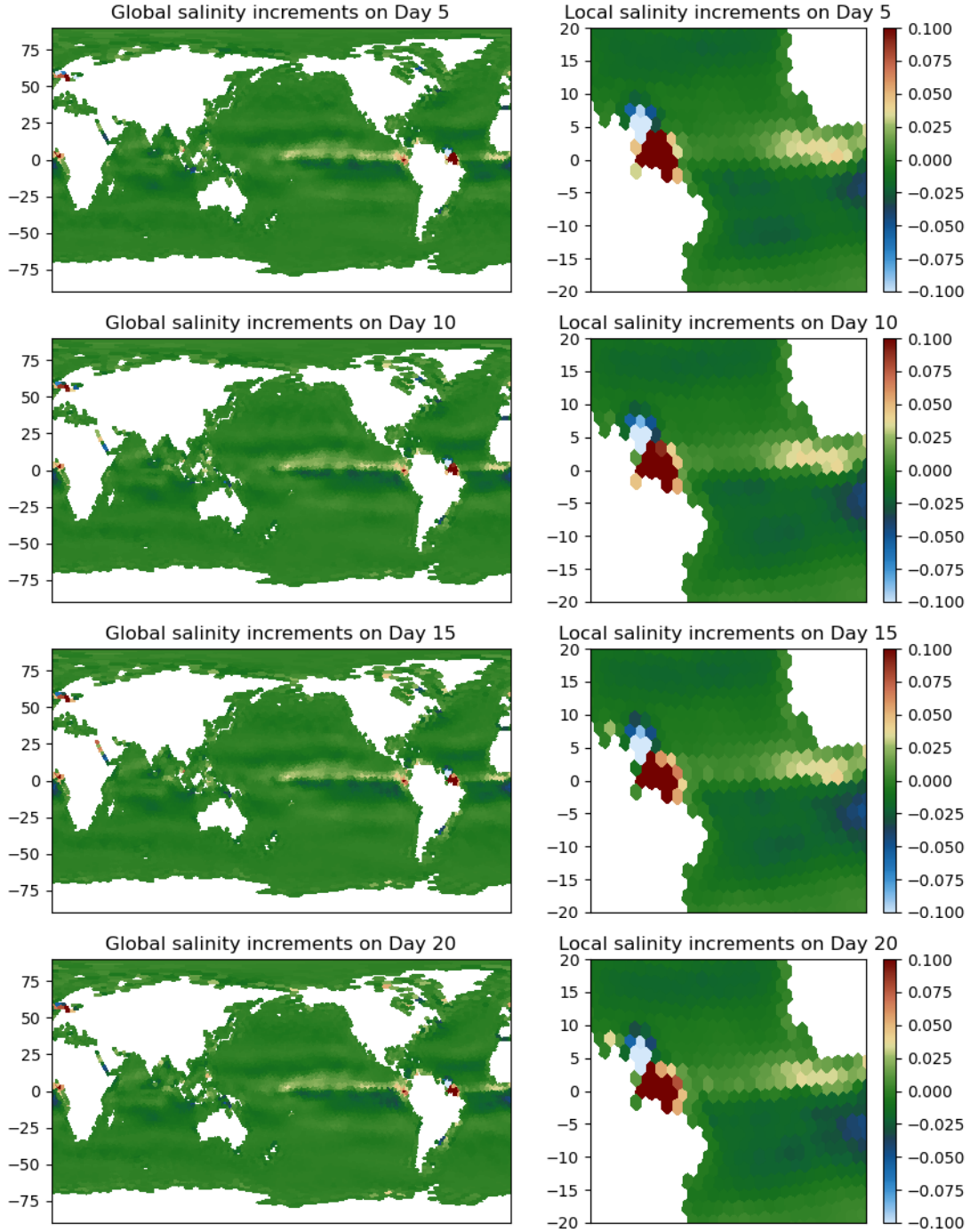


Figure 5: Simulated salinity increments using the SSPRK3-SE scheme with $\Delta t = 256$ s, $M = 16$ for the global ocean test case. From top to bottom are the results on Day 5, 10, 15, and 20. The left ones are the global salinity increments, and the right ones are for the local area at latitude from 20°S to 20°N, and longitude extending east-ward between 60°W and 0°E.

composition is performed only along the horizontal directions, and consequently the unknowns from all layers but at the same vertical line stay in the same computing core. In addition to the QU240 mesh, we also consider another ocean mesh provided by the MPAS-Ocean platform, denoted there

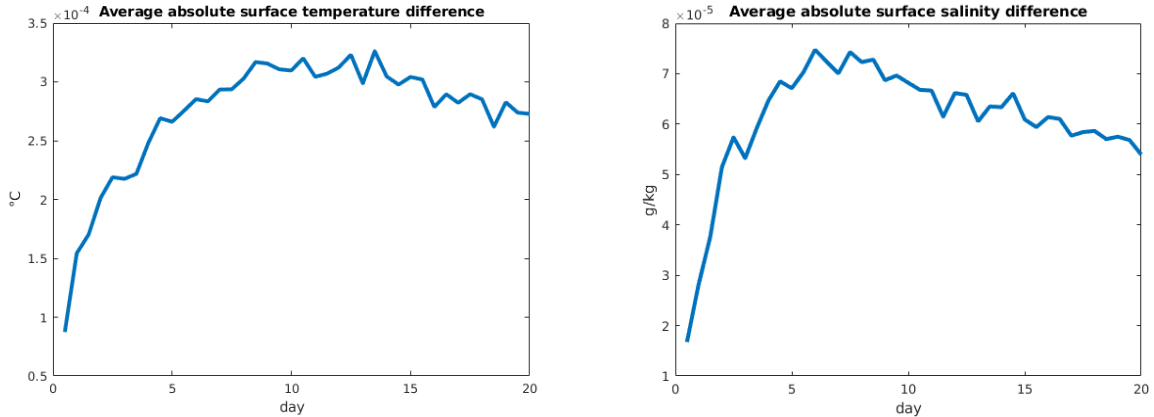


Figure 6: Evolutions of the average absolute differences between the simulated surface temperatures (left) and salinity (right) produced by using the SSPRK3-SE scheme (with vertical mixing) and MPAS-SE with $\Delta t = 256$ s and $M = 16$.

as “EC60to30”, which contains 60 vertical layers with horizontal resolution varying from 30 km at the equator and poles to 60 km at the mid-latitudes. The grid consists of 235,160 cells, 714,274 edges, and 478,835 vertices at each layer. We set $\Delta t = 128$ s and $M = 16$ in all simulations. The tests on the QU240 mesh use up to 64 cores and those on the EC60to30 mesh up to 256 cores. The plots of the running time per step vs. the number of cores and the corresponding speedups are presented in Figure 7. We see that in practice the SSPRK-SE schemes with vertical mixing just cost a little bit more than the SSPRK-SE schemes without vertical mixing. All schemes show very good parallel scalability, and at the same time, the larger the used spatial mesh is, the better the parallel performance is gained as expected.

6. Conclusions

This paper is concerned with the numerical solution of the barotropic and baroclinic dynamic split system for the layered primitive equations. We designed high-order multirate explicit time-stepping schemes based on the strong stability preserving Runge-Kutta method. In particular, second- and third-order schemes (SSPRK2-SE and SSPRK3-SE, respectively) are proposed and analyzed in detail. Numerical tests on two benchmark test problems from the MPAS-Ocean platform are also performed to demonstrate the accuracy and performance of the proposed schemes. On the other hand, we also show that the overall approximation accuracies still could be restricted by other sources of error, including spatial discretization errors, mode splitting errors and errors introduced by vertical mixing. These error terms are tangled up so that a thorough analysis is not an easy task. As the next step, we plan to design higher-order operator splitting schemes for the vertical mixing techniques that will not affect the corresponding convergence orders when combined with the proposed schemes. Also, incorporating tracer solves into the proposed schemes without losing high-order temporal accuracy remains another important task to consider. In addition, it would be very interesting and useful to design high-order explicit-implicit (explicit for the baroclinic modes and implicit for the barotropic mode) time-stepping schemes so that large global uniform time-stepping can be used for the split system.

Acknowledgement

This work was supported by the U.S. Department of Energy, Office of Science, Office of Biological and Environmental Research through Earth and Environmental System Modeling and Scientific

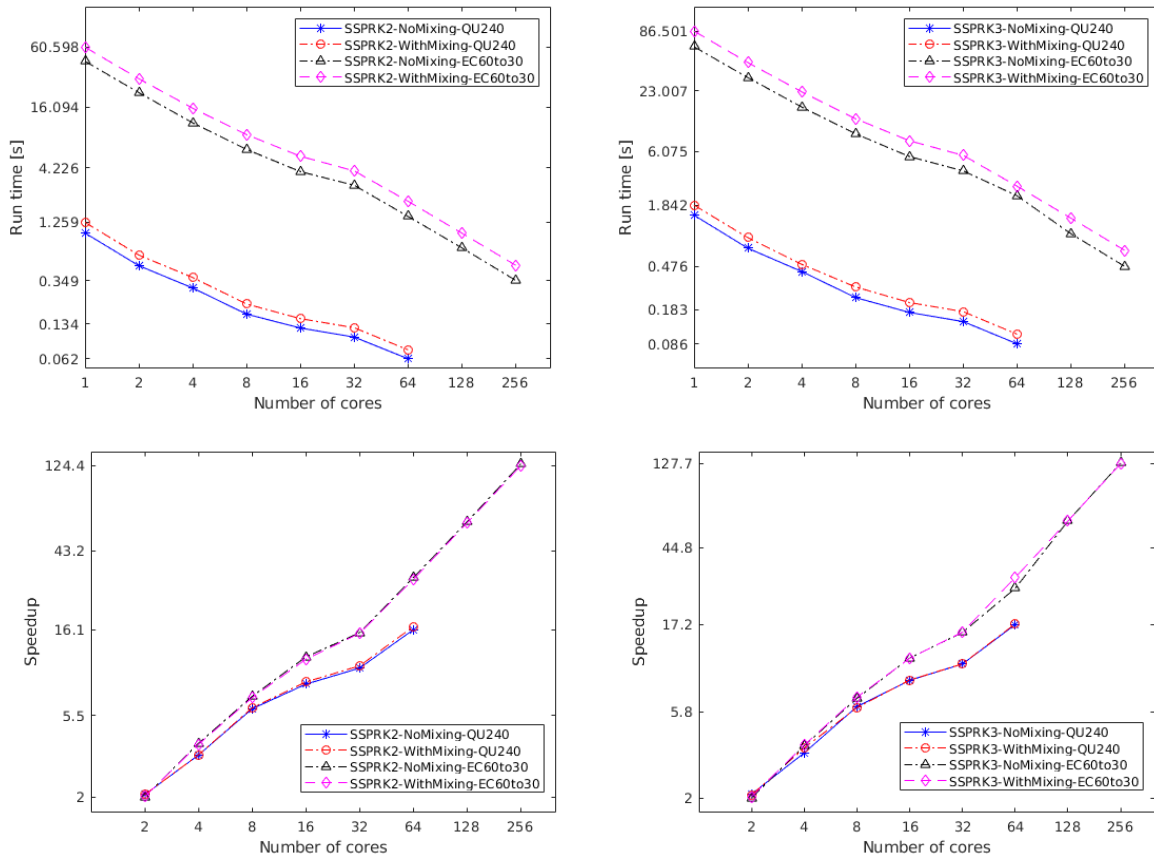


Figure 7: Plots of the run times per step vs. the number of cores (top row) and the corresponding parallel speedups (bottom row) for the global ocean test case using two different global ocean meshes. Left: the SSPRK2-SE scheme with or without mixing; right: the SSPRK3-SE scheme with or without mixing.

Discovery through Advanced Computing programs at Los Alamos National Laboratory and under university grants DE-SC0020270 and DE-SC0020418. This research used the computing resources of National Energy Research Scientific Computing Center, a U.S. Department of Energy Office of Science User Facility operated under Contract No. DE-AC02-05CH11231.

References

- [1] C. Chen, H. Liu, R. C. Beardsley, An unstructured grid, finite-volume, three-dimensional, primitive equations ocean model: Application to coastal ocean and estuaries, *Journal of Atmospheric and Oceanic Technology* 20 (1) (2003) 159–186.
- [2] J. Smagorinsky, General circulation experiments with the primitive equations: I. The basic experiment, *Monthly Weather Review* 91 (3) (1963) 99–164.
- [3] G. K. Vallis, *Atmospheric and Oceanic Fluid Dynamics*, Cambridge University Press, Cambridge, U.K., 2006.
- [4] I. Kinnmark, *The Shallow Water Wave Equations: Formulation, Analysis and Application*, Vol. 15 of *Lecture Notes in Engineering*, Springer-Verlag, New York, 2012.

- [5] C. B. Vreugdenhil, Numerical methods for shallow-water flow, Vol. 13 of Water Science and Technology Library, Kluwer Academic Publishers, Dordrecht, 1994.
- [6] B. Cushman-Roisin, J.-M. Beckers, Introduction to Geophysical Fluid Dynamics: Physical and Numerical Aspects, Vol. 101 of International Geophysics Series, Academic Press, Amsterdam, 2011.
- [7] J. Diaz, M. J. Grote, Energy conserving explicit local time stepping for second-order wave equations, *SIAM Journal on Scientific Computing* 31 (3) (2009) 1985–2014.
- [8] T.-T.-P. Hoang, L. Ju, W. Leng, Z. Wang, High order explicit local time stepping methods for hyperbolic conservation laws, *Mathematics of Computation* 89 (324) (2020) 1807–1842.
- [9] T.-T.-P. Hoang, W. Leng, L. Ju, Z. Wang, K. Pieper, Conservative explicit local time-stepping schemes for the shallow water equations, *Journal of Computational Physics* 382 (2019) 152–176.
- [10] C. J. Trahan, C. Dawson, Local time-stepping in Runge–Kutta discontinuous Galerkin finite element methods applied to the shallow-water equations, *Computer Methods in Applied Mechanics and Engineering* 217 (2012) 139–152.
- [11] R. Bleck, L. T. Smith, A wind-driven isopycnic coordinate model of the north and equatorial Atlantic Ocean: 1. Model development and supporting experiments, *Journal of Geophysical Research: Oceans* 95 (C3) (1990) 3273–3285.
- [12] R. L. Higdon, Implementation of a barotropic–baroclinic time splitting for isopycnic coordinate ocean modeling, *Journal of Computational Physics* 148 (2) (1999) 579–604.
- [13] R. L. Higdon, A two-level time-stepping method for layered ocean circulation models, *Journal of Computational Physics* 177 (1) (2002) 59–94.
- [14] R. L. Higdon, A two-level time-stepping method for layered ocean circulation models: further development and testing, *Journal of Computational Physics* 206 (2) (2005) 463–504.
- [15] K. Bryan, A numerical method for the study of the circulation of the world ocean, *Journal of Computational Physics* 135 (2) (1997) 154–169.
- [16] J. K. Dukowicz, R. D. Smith, Implicit free-surface method for the Bryan-Cox-Semtner ocean model, *Journal of Geophysical Research: Oceans* 99 (C4) (1994) 7991–8014.
- [17] R. L. Higdon, R. A. de Szoeke, Barotropic-baroclinic time splitting for ocean circulation modeling, *Journal of Computational Physics* 135 (1) (1997) 30–53.
- [18] P. D. Killworth, D. J. Webb, D. Stainforth, S. M. Paterson, The development of a free-surface Bryan–Cox–Semtner ocean model, *Journal of Physical Oceanography* 21 (9) (1991) 1333–1348.
- [19] A. F. Shchepetkin, J. C. McWilliams, The regional oceanic modeling system (ROMS): A split-explicit, free-surface, topography-following-coordinate oceanic model, *Ocean Modelling* 9 (4) (2005) 347–404.
- [20] R. L. Higdon, A. F. Bennett, Stability analysis of operator splitting for large-scale ocean modeling, *Journal of Computational Physics* 123 (2) (1996) 311–329.

- [21] T. Ringler, M. Petersen, R. L. Higdon, D. Jacobsen, P. W. Jones, M. Maltrud, A multi-resolution approach to global ocean modeling, *Ocean Modelling* 69 (2013) 211–232.
- [22] J.-C. Golaz, P. M. Caldwell, L. P. Van Roekel, M. R. Petersen, Q. Tang, J. D. Wolfe, G. Abeshu, V. Anantharaj, X. S. Asay-Davis, D. C. Bader, S. A. Baldwin, G. Bisht, P. A. Bogenschutz, M. Branstetter, M. A. Brunke, S. R. Brus, S. M. Burrows, P. J. Cameron-Smith, A. S. Donahue, M. Deakin, R. C. Easter, K. J. Evans, Y. Feng, M. Flanner, J. G. Foucar, J. G. Fyke, B. M. Griffin, C. Hannay, B. E. Harrop, M. J. Hoffman, E. C. Hunke, R. L. Jacob, D. W. Jacobsen, N. Jeffery, P. W. Jones, N. D. Keen, S. A. Klein, V. E. Larson, L. R. Leung, H.-Y. Li, W. Lin, W. H. Lipscomb, P.-L. Ma, S. Mahajan, M. E. Maltrud, A. Mametjanov, J. L. McClean, R. B. McCoy, R. B. Neale, S. F. Price, Y. Qian, P. J. Rasch, J. E. J. Reeves Eyre, W. J. Riley, T. D. Ringler, A. F. Roberts, E. L. Roesler, A. G. Salinger, Z. Shaheen, X. Shi, B. Singh, J. Tang, M. A. Taylor, P. E. Thornton, A. K. Turner, M. Veneziani, H. Wan, H. Wang, S. Wang, D. N. Williams, P. J. Wolfram, P. H. Worley, S. Xie, Y. Yang, J.-H. Yoon, M. D. Zelinka, C. S. Zender, X. Zeng, C. Zhang, K. Zhang, Y. Zhang, X. Zheng, T. Zhou, Q. Zhu, The DOE E3SM Coupled Model Version 1: Overview and Evaluation at Standard Resolution, *Journal of Advances in Modeling Earth Systems* 11 (7) (2019) 2089–2129.
- [23] M. R. Petersen, X. S. Asay-Davis, A. S. Berres, Q. Chen, N. Feige, M. J. Hoffman, D. W. Jacobsen, P. W. Jones, M. E. Maltrud, S. F. Price, T. D. Ringler, G. J. Streltetz, A. K. Turner, L. P. V. Roekel, M. Veneziani, J. D. Wolfe, P. J. Wolfram, J. L. Woodring, An Evaluation of the Ocean and Sea Ice Climate of E3SM Using MPAS and Interannual CORE-II Forcing, *Journal of Advances in Modeling Earth Systems* 11 (5) (2019) 1438–1458.
- [24] S. M. Reckinger, M. R. Petersen, S. J. Reckinger, A study of overflow simulations using MPAS-Ocean: Vertical grids, resolution, and viscosity, *Ocean Modelling* 96 (2015) 291–313.
- [25] P. J. Wolfram, T. D. Ringler, M. E. Maltrud, D. W. Jacobsen, M. R. Petersen, Diagnosing isopycnal diffusivity in an eddying, idealized midlatitude ocean basin via Lagrangian, In situ, Global, High-Performance particle Tracking (LIGHT), *Journal of Physical Oceanography* 45 (8) (2015) 2114–2133.
- [26] J. Woodring, M. Petersen, A. Schmeisser, J. Patchett, J. Ahrens, H. Hagen, In situ eddy analysis in a high-resolution ocean climate model, *IEEE transactions on visualization and computer graphics* 22 (1) (2015) 857–866.
- [27] M. R. Petersen, X. S. Asay-Davis, D. W. Jacobsen, M. E. Maltrud, T. D. Ringler, L. Van Roekel, C. Veneziani, P. J. Wolfram Jr, *MPAS-Ocean Model User’s Guide, Version 6.0* (2018).
URL <https://zenodo.org/record/1246893#.WvsFwNMvzMU>
- [28] T. D. Ringler, J. Thuburn, J. B. Klemp, W. C. Skamarock, A unified approach to energy conservation and potential vorticity dynamics for arbitrarily-structured C-grids, *Journal of Computational Physics* 229 (9) (2010) 3065–3090.
- [29] J. Thuburn, T. D. Ringler, W. C. Skamarock, J. B. Klemp, Numerical representation of geostrophic modes on arbitrarily structured C-grids, *Journal of Computational Physics* 228 (22) (2009) 8321–8335.
- [30] M. Günther, A. Kvaernø, P. Rentrop, Multirate partitioned Runge-Kutta methods, *BIT Numerical Mathematics* 41 (3) (2001) 504–514.

- [31] E. Hairer, S. P. Nørsett, G. Wanner, Solving Ordinary Differential Equations I, Nonstiff Problems, Vol. 8 of Springer Series in Computational Mathematics, Springer-Verlag, Berlin, 1993.
- [32] A. Sandu, M. Günther, A generalized-structure approach to additive Runge–Kutta methods, *SIAM Journal on Numerical Analysis* 53 (1) (2015) 17–42.
- [33] M. Günther, A. Sandu, Multirate generalized additive Runge Kutta methods, *Numerische Mathematik* 133 (3) (2016) 497–524.
- [34] S. M. Griffies, C. Böning, F. O. Bryan, E. P. Chassignet, R. Gerdes, H. Hasumi, A. Hirst, A.-M. Treguier, D. Webb, Developments in ocean climate modelling, *Ocean Modelling* 2 (3-4) (2000) 123–192.
- [35] C.-W. Shu, Total-variation-diminishing time discretizations, *SIAM Journal on Scientific and Statistical Computing* 9 (6) (1988) 1073–1084.
- [36] R. J. LeVeque, Numerical methods for conservation laws, Vol. 132 of Lectures in Mathematics ETH Zurich, Birkhäuser, Basel, 1992.
- [37] S. Gottlieb, C.-W. Shu, Total variation diminishing Runge-Kutta schemes, *Mathematics of Computation* 67 (221) (1998) 73–85.
- [38] S. Gottlieb, C.-W. Shu, E. Tadmor, Strong stability-preserving high-order time discretization methods, *SIAM Review* 43 (1) (2001) 89–112.
- [39] S. Gottlieb, D. I. Ketcheson, C.-W. Shu, Strong Stability Preserving Runge-Kutta and Multi-step Time Discretizations, World Scientific, Singapore, 2011.
- [40] J. Pietrzak, The use of TVD limiters for forward-in-time upstream-biased advection schemes in ocean modeling, *Monthly Weather Review* 126 (3) (1998) 812–830.
- [41] F. Shi, J. T. Kirby, J. C. Harris, J. D. Geiman, S. T. Grilli, A high-order adaptive time-stepping TVD solver for Boussinesq modeling of breaking waves and coastal inundation, *Ocean Modelling* 43 (2012) 36–51.
- [42] H. Weller, S.-J. Lock, N. Wood, Runge–Kutta IMEX schemes for the horizontally explicit/vertically implicit (HEVI) solution of wave equations, *Journal of Computational Physics* 252 (2013) 365–381.
- [43] G. H. Golub, C. F. Van Loan, Matrix Computations, Vol. 3, The Johns Hopkins University Press, Baltimore, 2013.
- [44] S. M. Griffies, M. Levy, A. J. Adcroft, G. Danabasoglu, R. W. Hallberg, D. Jacobsen, W. Large, T. Ringler, [Theory and numerics of the community ocean vertical mixing \(CVMix\) project](#), Tech. Rep.
URL <https://github.com/CVMix/CVMix-description/blob/master/cvmix.pdf>
- [45] J. Thuburn, C. J. Cotter, A framework for mimetic discretization of the rotating shallow-water equations on arbitrary polygonal grids, *SIAM Journal on Scientific Computing* 34 (3) (2012) B203–B225.
- [46] M. Ilıcak, A. J. Adcroft, S. M. Griffies, R. W. Hallberg, Spurious dianeutral mixing and the role of momentum closure, *Ocean Modelling* 45 (2012) 37–58.

- [47] Q. Du, M. Gunzburger, L. Ju, Constrained Centroidal Voronoi Tessellations for Surfaces, SIAM Journal on Scientific Computing 24 (22003) 1488–1506.
- [48] X. Asay-Davis, M. Veneziani, P. J. Wolfram, L. V. Roedel, D. Comeau, R. Brady, J. H. Kennedy, G. Streletz, S. Price, A. K. Turner, Kevin, M. Petersen, M. Hoffman, C. Doutriaux, MPAS-Dev/MPAS-Analysis: v1.2.2 (Mar. 2019).
URL <https://doi.org/10.5281/zenodo.2586240>
- [49] F. Samsel, T. L. Turton, R. Bujack, D. H. Rogers, J. Ahrens, G. Abram, C. Ware, Data science at scale sci-vis color website (2020).
URL <https://sciviscolor.org>